The Astrophysical Journal, 936:110 (20pp), 2022 September 10 https://doi.org/10.3847/1538-4357/ac854c
© 2022. The Author(s). Published by the American Astronomical Society.
OPEN ACCESS

The Physical Properties of Low-redshift FeLoBAL Quasars. III. The Location and Geometry of the Outflows

Hyunseop Choi (최현섭)[1], Karen M. Leighly[1], Collin Dabbieri[1,2], Donald M. Terndrup[1,3], Sarah C. Gallagher[4,5,6,7], and Gordon T. Richards[8]

[1] Homer L. Dodge Department of Physics and Astronomy, The University of Oklahoma, 440 W. Brooks Street, Norman, OK 73019, USA; hyunseop.choi@ou.edu
[2] Department of Physics and Astronomy, Vanderbilt University, 2301 Vanderbilt Place, Nashville, TN 37235-1807, USA
[3] Department of Astronomy, The Ohio State University, 140 W. 18th Avenue, Columbus, OH 43210, USA
[4] Department of Physics & Astronomy, The University of Western Ontario, London, ON, N6A 3K7, Canada
[5] Canadian Space Agency, 6767 Route de l'Aéroport, Saint-Hubert, Quebec, J3Y BY9, Canada
[6] Institute for Earth and Space Exploration, The University of Western Ontario, London, ON, N6A 3K7, Canada
[7] The Rotman Institute of Philosophy, The University of Western Ontario, London, ON, N6A 3K7, Canada
[8] Department of Physics, Drexel University, 32 S. 32nd Street, Philadelphia, PA 19104, USA
Received 2022 January 16; revised 2022 July 20; accepted 2022 July 27; published 2022 September 7

Abstract

We present continued analysis of a sample of low-redshift iron low-ionization broad-absorption-line quasars (FeLoBALQs). Choi et al. presented *SimBAL* spectral analysis of broad-absorption-line (BAL) outflows in 50 objects. Leighly et al. analyzed the optical emission lines of 30 of those 50 objects and found that they are characterized by either a high accretion rate ($L_{\rm Bol}/L_{\rm Edd} > 0.3$) or low accretion rate ($0.03 < L_{\rm Bol}/L_{\rm Edd} < 0.3$). We report that the outflow velocity is inversely correlated with the BAL location among the high-accretion-rate objects, with the highest velocities observed in parsec-scale outflows. In contrast, the low-Eddington-ratio objects showed the opposite trend. We confirmed the known relationship between the outflow velocity and $L_{\rm Bol}/L_{\rm Edd}$ and found that the scatter plausibly originates in the force multiplier (launch radius) in the low(high)-accretion-rate objects. A log volume filling factor between -6 and -4 was found in most outflows but was as high as -1 for low-velocity compact outflows. We investigated the relationship between the observed [O III] emission and that predicted from the BAL gas. We found that these could be reconciled if the emission-line covering fraction depends on the Seyfert type and BAL location. The difference between the predicted and observed [O III] luminosity is correlated with the outflow velocity, suggesting that [O III] emission in high-Eddington-ratio objects may be broad and hidden under Fe II emission. We suggest that the physical differences in the outflow properties as a function of location in the quasar and accretion rate point to different formation, acceleration, and confinement mechanisms for the two FeLoBALQ types.

Unified Astronomy Thesaurus concepts: Broad-absorption line quasar (183); Quasars (1319); Active galactic nuclei (16)

1. Introduction

The broad and blueshifted C IV $\lambda\lambda$1548, 1551 lines observed in broad absorption-line quasars (BALQs) reveal the unambiguous signature of outflows. Therefore, BALQs may be important sources of quasar feedback in galaxy evolution. In this context, an important parameter is the ratio of the kinetic luminosity ($L_{\rm KE}$) to bolometric luminosity ($L_{\rm Bol}$), because it has been shown that if $L_{\rm KE}/L_{\rm Bol}$ exceeds 0.5%–5% (Di Matteo et al. 2005; Hopkins & Elvis 2010) then sufficient energy is available to regulate star formation and therefore produce the distribution of galaxies that we see today.

Determining $L_{\rm KE}/L_{\rm Bol}$ in the general population of BALQs is challenging. The measurement of $L_{\rm KE}$ requires constraint of key physical parameters of the outflowing gas including the column density N_H, the velocity, and the location of the outflow, as well as an estimate of Ω, the fraction of the full 4π steradians that is covered by the outflow. The velocity can be estimated from the blueshift of the absorption lines, and Ω is estimated from the incidence of BAL quasars in the population. The column density and location require measurement of the photoionization properties of the outflowing gas. These properties can be inferred directly from measurements of the optical depths of absorption lines in the spectrum, but only when the lines are relatively narrow and line blending is not severe. This approach has been used on some tens of spectra (e.g., Arav et al. 2020; Miller et al. 2020, and references therein).

However, this type of analysis cannot be done on spectra in which line blending is significant, i.e., most of the ~30,000 BAL quasar spectra present in the Sloan Digital Sky Survey (SDSS) data release 14 Quasar (DR14Q) archive (Pâris et al. 2018). It is easy to understand why we cannot generalize results from 10 s of spectra with narrow absorption lines to the quasar population in general. The kinetic luminosity depends principally on the outflow velocity, as that factor enters the equation for $L_{\rm KE}$ to the cubed power. Moreover, observations show that BAL velocities have a tremendous range, from nearly zero velocity or inflow in a few cases to more than 30,000 km s^{-1}. At high velocities, blending is usually significant. Samples of BAL quasars repeatedly show a relationship between the BAL outflow velocity and the luminosity of the quasar (e.g., Laor & Brandt 2002; Ganguly et al. 2007), but the dependence is complicated, with the relationship showing an upper-limit envelope rather than a one-to-one dependence.

Original content from this work may be used under the terms of the Creative Commons Attribution 4.0 licence. Any further distribution of this work must maintain attribution to the author(s) and the title of the work, journal citation and DOI.

So, we can expect that a powerful quasar located at $z = 2$–3 that may have a bolometric luminosity exceeding 10^{48} erg s^{-1} will have much different outflow properties and L_{KE}/L_{Bol} than a Seyfert luminosity object at $z = 0.5$–1.5.

It is also very plausible that L_{KE}/L_{Bol} depends on the Eddington ratio L_{Bol}/L_{Edd} of the quasar. The terminal velocity of an accelerated outflow depends on the magnitude of the acceleration but also on the deceleration due to gravity provided by the supermassive black hole. Also, we expect the geometry and physical conditions of the central engine to change with this parameter (e.g., Giustini & Proga 2019). Finally, we infer profound dependence of the broad emission lines on L_{Bol}/L_{Edd} and ask why the absorption lines should not also depend on this factor. The bottom line is that it is probably not reasonable to expect a single value of L_{KE}/L_{Bol} to be applicable to all UV outflows, but rather that this parameter should depend on (at least) the luminosity (equivalently the black hole mass) and the Eddington ratio.

A first step in making progress on the relationships between fundamental quasar parameters and outflow properties would be to analyze broad absorption lines from many more objects representing the full range of the BAL phenomena. This step requires a method to handle line blending. Here, we use the term "line blending" to mean that the velocity width of the broad absorption lines is sufficiently large that different absorption lines blend together regardless of the spectral resolution. That problem is now approachable using the novel spectral synthesis code *SimBAL*. The *SimBAL* methodology is described in Leighly et al. (2018). *SimBAL* uses a forward modeling method. It creates synthetic spectra parameterized by photoionization conditions of the outflowing gas and then compares them with the observed spectrum using a Markov Chain Monte Carlo (MCMC) method (`emcee`; Foreman-Mackey et al. 2013). Additional examples of the use of *SimBAL* can be found in Leighly et al. (2019b) and Choi et al. (2020). The *SimBAL* analysis of the objects described in this paper is found in Choi et al. (2022).

The second thing we can do is to try to understand the physics of BAL outflows. If that could be done, then we could predict the outflow properties in a given quasar, given its (say) luminosity and Eddington ratio. Despite 50 years of study, it is still not known how these outflows are accelerated, what confines the BAL "clouds", or what the origin of the absorbing gas is. In short, the same questions that were posed in the '80 s and '90 s are still unanswered and are still relevant today.

Some of these questions can be addressed by studying the rest-frame optical emission lines in BAL quasars. First, the Hβ λ4863 Å emission-line region yields an estimate of the black hole mass. Black hole mass estimates are also available using Mg II $\lambda\lambda$2796, 2804 (e.g., Bahk et al. 2019), and C IV (e.g., Coatman et al. 2017), but those lines may be significantly absorbed in BAL quasars, a fact that adds significant uncertainty. In contrast, it is rare to observe absorption in Balmer lines and even when they are present in the spectra, the Balmer emission lines (e.g., Hβ) generally are not significantly absorbed and can be easily studied (e.g., Schulze et al. 2018). The Hβ region also includes [O III]λ4960, 5008, and many thousands of lines in the Fe II pseudocontinuum emission, and together with Hβ, these parameters are thought to reflect the physical conditions of the central engine through a pattern of behavior known as Eigenvector 1 (Boroson & Green 1992), which is widely considered to be a probe of the Eddington ratio. Eigenvector 1 is repeatedly found in principal components analysis (PCA) of optical rest-frame quasar spectra (e.g., Grupe 2004; Ludwig et al. 2009; Wolf et al. 2020). Thus, we might expect that, just as we observed the BAL outflow velocity to depend on the quasar luminosity, we should expect BAL properties to depend on the Eigenvector 1 properties.

BAL quasars are divided into three types based on the absorption lines present in the spectrum. C IV is the most commonly observed line, observed in 10%–26% of optically selected quasars (Tolea et al. 2002; Hewett & Foltz 2003; Reichard et al. 2003; Trump et al. 2006; Knigge et al. 2008; Gibson et al. 2009). Objects that only have this line plus other high-ionization lines such as N V $\lambda\lambda$1239, 1242 and Si IV $\lambda\lambda$1394, 1403 are called high-ionization broad-absorption-line quasars (HiBALQs). About 1.3% of quasars have broad Mg II absorption (Trump et al. 2006); these are called low-ionization broad-absorption-line quasars (LoBALQs). About 0.3% of quasars also have absorption from Fe II, and these are called iron low-ionization broad-absorption-line (FeLoBAL) quasars (FeLoBALQs; Trump et al. 2006). These objects are observed much less frequently than the other two categories, but to some extent, their rarity can be attributed to the difficulties in detecting these objects, as they may lack strong emission lines due to absorption. Furthermore, their spectral energy distributions (SEDs) show the reddest colors among BAL quasars, which suggests that they may represent a short-lived stage in quasar evolution where the quasar expels its cocoon of gas and dust ("blowout" phase; e.g., Sanders et al. 1988), transitioning from the ultraluminous infrared galaxy (ULIRG) phase (e.g., Urrutia et al. 2009; Glikman 2017; Glikman et al. 2018). Finally, the physical conditions of the outflow gas can be particularly well constrained using the thousands of Fe II absorption lines.

This paper is the third in a sequence of four papers reporting the results of a comprehensive analysis of a sample of FeLoBALQs. Paper I (Choi et al. 2022) describes a sample of 50 low-redshift ($0.66 \leqslant z \leqslant 1.63$) FeLoBALQs and the *SimBAL* spectral synthesis analysis of their absorption lines. That work represents an increase by a factor of 5 in FeLoBALQs with detailed photoionization analysis. We measured the velocity and velocity width, the ionization parameter, density, column density, and covering fraction directly from the spectra. We extracted the location of the outflow, as well as the mass outflow rate and energetics of the outflow. We found that FeLoBAL outflows cover a large range of outflow locations in a quasar, spanning $\log R$ between 0 and 4.4 [pc]. While many of the troughs were well described by a single outflow component characterized by a single ionization parameter and density, about 20% of the objects showed evidence of multiple troughs, where the higher-velocity components generally had higher ionization parameters. Among these objects, several special classes of BAL outflows were found. Overlapping trough objects (e.g., Hall et al. 2002) show broad absorption troughs that blanket the near-UV shortward of Mg II. All of these objects were found to have compact outflows with $\log R < 1$ [pc]. Among these objects, we discovered a new type of FeLoBALQs. Dubbed "loitering" outflow FeLoBALQs, these objects generally have narrow lines and low velocities and are also compact with $\log R < 1$ [pc]. They are distinguished from the other overlapping trough objects not only by their velocity width but also their tendency to have a higher ionization parameter and higher density gas

(Figure 6 of Choi et al. 2022), which lead to opacity from many high-excitation states. The outflowing gas in about half of these objects occults only the continuum-emission region but not the broad emission lines. The remaining objects were located farther from the quasar and generally did not have extreme properties. We also found that there was a significant correlation between the color of the quasar UV–near-IR SED and the outflow strength where quasars with redder SEDs have more energetic outflows. Finally, we discussed how the potential acceleration mechanisms and the origins of the FeLoBAL winds may differ for outflows at different locations in the quasars.

Thirty of the fifty FeLoBALQs analyzed in Choi et al. (2022) have sufficiently low redshift that the Hβ emission-line region is present at the red end of the SDSS spectra. Paper II of Leighly et al. (2022) describes the rest-frame optical emission-line analysis of this subsample, along with a 132 object comparison sample of non-BAL quasars. The principal result of that paper is that FeLoBALQs are divided into two classes based on their emission-line properties, and their emission-line properties are distributed differently than those of the comparison sample. Specifically, FeLoBALQs were characterized by either weak Fe II relative to Hβ and strong [O III], or strong Fe II relative to Hβ and weak [O III], and intermediate values were avoided. Further analysis revealed that the emission-line properties reflect the accretion rate relative to the Eddington limit. Therefore, FeLoBALQs at low redshift are characterized by either high Eddington ratios (typically greater than 1), a result that agrees with previous analysis of BAL quasars (Yuan & Wills 2003; Boroson 2002; Runnoe et al. 2013), or low Eddington ratios (typically less than 0.1), a new result, but are uncommon at the intermediate Eddington ratios that are the most prevalent in the comparison sample. The fact that their emission-line properties are different than those of unabsorbed quasars shows that among low-redshift and low-luminosity objects, FeLoBAL and non-BAL quasars do not have the same parent sample. This result is different than what has been recently reported for high-ionization broad-absorption-line (HiBAL) quasars, which have higher luminosities (Rankine et al. 2020).

This paper combines the *SimBAL* results of Choi et al. (2022) and emission-line analysis results of the 30 object subsample from Leighly et al. (2022) to search for relationships between the properties of the outflowing gas and the properties of the central engine. Choi et al. (2022) demonstrated that the BAL outflow velocity is related to the bolometric luminosity in the 50 object sample, as has been found previously (e.g., Laor & Brandt 2002; Ganguly et al. 2007; Fiore et al. 2017). However, *SimBAL* delivers quite a bit more information characterizing the outflow than typical BAL analyses, including the parameters describing the ionization state, density, column density, and covering fraction, but also the location of the outflow. We therefore take the first steps in tackling the question posed above and examine how the location, geometry, confinement, and other properties of the outflowing gas depend on the global quasar properties such as the luminosity and Eddington ratio.

The final paper in the series, Paper IV (K. M. Leighly et al. 2022, in preparation), includes an analysis of the broadband optical/IR properties and discusses the potential implications for quasar evolution scenarios.

This paper is organized as follows. In Section 2 we briefly describe the data extracted from Choi et al. (2022) and Leighly et al. (2022). We principally focused on the 30 object $z < 1$ subsample for which the Hβ region is available and the analysis described in Leighly et al. (2022), although we also explored the volume filling factor in the full sample. In Section 3, we used the $E1$ parameter defined in Leighly et al. (2022) to divide the FeLoBALQs into high- and low-accretion-rate objects and then compared the *SimBAL* properties of the two classes. We also correlated the *SimBAL* parameters with one another, and with the optical emission-line and global parameters. Finally, we investigated the relationship between the properties of the observed [O III] emission lines and the [O III] emission predicted to originate in the BAL gas. Section 5 presents a summary of the results.

We used cosmological parameters $\Omega_\Lambda = 0.7$, $\Omega_M = 0.3$, and $H_0 = 70\ \mathrm{km\ s^{-1}\ Mpc^{-1}}$, unless otherwise specified.

2. Data

The data used in this paper are described in detail in Papers I (Choi et al. 2022) and II (Leighly et al. 2022). The *SimBAL* model-fitting results were drawn from Paper I, and the optical emission-line modeling and global properties were taken from Paper II. Those parameters are described briefly in the next sections.

2.1. SimBAL Parameters

The *SimBAL* model fits for the sample are given in Choi et al. (2022), and the details can be found in that paper (Tables 2 and 3). We extracted the following parameters from those results: the ionization parameter $\log U$, the gas density $\log n$ [$\mathrm{cm^{-2}}$], the broad-absorption-line velocity $V_{\rm off}$ ($\mathrm{km\ s^{-1}}$), the broad-absorption-line velocity width V_{width} ($\mathrm{km\ s^{-1}}$)[9], the total column density integrated over the BAL feature $\log N_H$ [$\mathrm{cm^{-2}}$], the covering-fraction parameter $\log a$, and the radius of the outflow $\log R$ [pc].

Several additional and derived parameters were also produced that are not reported in tables in Choi et al. (2022). These include the largest and smallest outflow velocities V_{max}, V_{min}, the force multiplier (FM; the ratio of the total opacity to the electron scattering opacity), the thickness of the outflow ΔR [pc], the filling factor $\log \Delta R/R$, the net outflow rate $\log \dot{M}$ [$M_\odot\ \mathrm{yr^{-1}}$] (per component), the net kinetic luminosity $\log L_{\rm KE}$ [$\mathrm{erg\ s^{-1}}$], and the ratio of the net kinetic luminosity to the bolometric luminosity. The thickness of the outflow ΔR is the ratio of the total column density and the density. Making the simple assumption that the azimuthal size of the outflowing gas is comparable to the thickness of the gas (i.e., the gas is distributed into individual clouds and the clouds are approximately spherical), and using the radius of the accretion disk at 2800 Å described in Leighly et al. (2022), we computed the log of the number of clouds required to cover the continuum-emission region (see Section 4.3.2 for more details).

Finally, we used the parameters from the *SimBAL* best-fitting solution to compute the luminosity of the predicted [O III] emission line assuming an emission-line global covering fraction of 0.1 (discussed in Section 4.4). We also computed

[9] The representative offset velocity is the median value of the MCMC chain after weighting by the true opacity. The true opacity is distinguished from the apparent opacity in that it takes into account partial covering of continuum- and emission-line-emitting region. The apparent opacity is extracted directly from the spectrum; see Choi et al. (2022) Section 4.1.3 for the definition. The minimum and maximum velocities and the velocity width were estimated from the 90% transmittance level from the model Mg II λ2796 velocity profile.

a parameter called the covering-fraction correction, described in that section, which parameterizes the comparison of the predicted [O III] luminosity from the wind with the observed [O III] luminosity.

2.2. Optical and Global Parameters

The following optical emission-line parameters were taken from Table 1 of Leighly et al. (2022). We used the Hβ FWHM and equivalent width to parameterize the Hβ line. Leighly et al. (2022) also defined a parameter called the Hβ deviation that measures the systematically broader Hβ FWHM observed among the FeLoBALQs compared with unabsorbed quasars. Fe II was parameterized using $R_{\rm FeII}$ defined as the ratio of the Fe II equivalent width in the range 4434–4684 Å to the broad Hβ equivalent width (e.g., Shen & Ho 2014). The [O III] emission line was parameterized using the equivalent width and luminosity, along with profile parameters v_{50} and w_{80} defined according to the prescription of Zakamska & Greene (2014). Briefly, from the normalized cumulative function of the broad [O III] model profile, the velocities at 0.1, 0.5, and 0.9 were identified. The velocity at 0.5 is assigned to v_{50}, and w_{80} is the difference between the velocities at 0.1 and 0.9. Leighly et al. (2022) also fit the FeLoBAL objects and the unabsorbed objects with eigenvectors created from the continuum-subtracted spectra of the unabsorbed objects (Section 2.3, Leighly et al. 2022). The fit coefficients for the first four eigenvectors (SPCA1–4) serve as a parameterization of the spectra. The first eigenvector displays the relationship between the strength of Fe II and [O III] that is commonly found (e.g., Grupe 2004; Ludwig et al. 2009; Wolf et al. 2020), and none of the other ones display any particular anomalies. We estimated the bolometric luminosity using the rest-frame flux density at 3 μm and a bolometric correction of 8.59 (Gallagher et al. 2007). BAL quasars tend to be reddened (e.g., Krawczyk et al. 2015), and evidence for reddening is present in this sample ($0 \lesssim E(B-V) \lesssim 0.5$; Figure 20 in Choi et al. 2022; K. M. Leighly et al. in preparation). Therefore, we used the 3 μm luminosity density as representative, rather than the luminosity in the optical or UV. The black hole mass and Eddington ratio were computed using standard methods and as described in Leighly et al. (2022; Section 2.1), and the calculation of the location of the 2800 Å emission from the accretion disk follows the method used in Leighly et al. (2019b).

Finally, we continue to use the $E1$ parameter, which was defined in Section 3.1 of Leighly et al. (2022). This parameter is a function of the measured values of $R_{\rm FeII}$ and the [O III] equivalent width. As described in Section 3.1 of Leighly et al. (2022), we normalized and scaled $R_{\rm FeII}$ and the [O III] equivalent width of the 132 object comparison sample and then derived the bisector line. We performed a coordinate rotation so that $E1$ is a parameter that lies along the bisector. Our $E1$ parameter is therefore related to the Boroson & Green (1992) Eigenvector 1. Boroson & Green (1992) performed a principal component analysis of the emission-line properties in the vicinity of Hβ and found that the variance is dominated by an anticorrelation between $R_{\rm FeII}$ and the [O III] equivalent width. Moreover, Eigenvector 1 has been shown to dominate the variance in quasar emission-line properties (e.g., Francis et al. 1992; Boroson & Green 1992; Brotherton et al. 1994; Corbin & Boroson 1996; Wills et al. 1999; Sulentic et al. 2000; Grupe 2004; Yip et al. 2004; Wang et al. 2006; Ludwig et al. 2009; Shen 2016). $E1$ is very strongly correlated with SPCA1 ($p = 6.5 \times 10^{-15}$ and $p = 10^{-50}$ for the FeLoBALQs and the unabsorbed comparison sample that was analyzed in parallel, respectively). It is also correlated with the Eddington ratio ($p = 1.2 \times 10^{-5}$ and $p = 9.3 \times 10^{-7}$ for the FeLoBALQs and the unabsorbed comparison sample, respectively). Here, p is a measure of the statistical significance of the correlation. More specifically, it is a probability that the observed correlation could have been produced from draws from two uncorrelated samples (e.g., Bevington 1969). A low (negative) value of the $E1$ parameter corresponds to a low accretion rate, while a high (positive) value of the $E1$ parameter corresponds to a high accretion rate. The 90% range of $\log L_{\rm bol}/L_{\rm Edd}$ among the sample is -1.4 to 0.84 (Figure 9 Leighly et al. 2022). As discussed in Section 3.3 of Leighly et al. (2022), the apparent bimodal distribution of FeLoBALQs in $E1$ shows that there are two types of FeLoBALQs: objects with $E1 < 0$ are characterized by a low Eddington ratio, and objects with $E1 > 0$ are characterized by a high Eddington ratio. We divided the FeLoBALQs into two groups based on this parameter, where the dividing line $E1 = 0$ corresponds to $\log L_{\rm Bol}/L_{\rm Edd} = -0.5$, i.e., an Eddington ratio of about 0.3. Throughout this paper, we use a consistent coloring scheme to denote $E1$: red (blue) corresponds to $E1 < 0$ and a low Eddington ratio ($E1 > 0$ and a high Eddington ratio).

3. Distributions and Correlations Between Optical and BAL Outflow Parameters

3.1. Distributions

Leighly et al. (2022) presented comparisons of the distributions of the emission-line and derived properties of the FeLoBALQs with those of the comparison sample of unabsorbed quasars using cumulative distribution plots. We applied the two-sample Kolmogorov–Smirnov (K-S) test, and the two-sample Anderson–Darling (A-D) test. The K-S test reliably tests the difference between two distributions when the difference is large at the median values, while the A-D test is more reliable if the differences lie toward the maximum or minimum values (i.e., the median can be the same, and the distributions different at larger and smaller values).[10] We also compared the samples divided by the sign of the $E1$ parameter. Note that the values of the $E1$ parameter and plots of the spectral model fits are given in Leighly et al. (2022). In this paper, we present the comparisons of the *SimBAL* parameters for the FeLoBALQs segregated by the $E1$ parameter (Table 1).

The results for the *SimBAL* parameters are shown in Figure 1, and the statistics are given in Table 1. The parameters that exhibit statistically significant differences between the $E1 > 0$ and $E1 < 0$ groups are all three velocity outflow parameters ($V_{\rm off}$, $V_{\rm max}$, and $V_{\rm min}$), the thickness of the outflow ΔR, the log filling factor, the log of the number of clouds covering the continuum-emitting source, and the covering-fraction correction factor. The $E1 > 0$ objects show systematically larger opacity-weighted outflow velocities than the $E1 < 0$ objects, with median values of $-1520\,{\rm km\,s^{-1}}$ and $-500\,{\rm km\,s^{-1}}$, respectively. For the $E1 < 0$ objects, the outflows are thicker, have larger filling fractions, and fewer[11] are required to cover the continuum source (median

[10] E.g., https://asaip.psu.edu/articles/beware-the-kolmogorov-smirnov-test/

[11] A median number of clouds less than zero might be interpreted as an approximately continuous outflow. Alternatively, a single cloud, if in the line of sight, would completely cover the continuum source.

Table 1
SimBAL E1 < 0 versus E1 > 0 Parameter Comparisons

Parameter Name	K-S[a] *Statistic/Probability*	A-D[b] *Statistic/Probability*
log$U$	0.21/0.28	0.64/0.18
log n [cm^{-3}]	0.24/0.57	−0.07/> 0.25
$V_{\rm offset}$ (km s^{-1})	**0.50/0.016**	**4.4/5.9 × 10^{-3}**
$V_{\rm max}$ (km s^{-1})	**0.50/0.014**	**4.2/7.0 × 10^{-3}**
$V_{\rm min}$ (km s^{-1})	**0.55/4.7×10^{-3}**	**5.0/3.6 × 10^{-3}**
$V_{\rm width}$ (km s^{-1})	0.30/0.33	0.67 / 0.17
log$a$	0.36/0.14	1.1/0.11
Net log $N_{\rm H}$ [cm^{-2}]	0.33/0.21	0.094/> 0.25
log Force Multiplier	0.35/0.17	0.32/> 0.25
log$R$ [pc]	0.26/0.45	−0.10/> 0.25
ΔR [pc]	**0.46/0.032**	**3.4/0.013**
log Volume Filling Factor	**0.51/9.8 × 10^{-3}**	**5.7/2.0 × 10^{-3}**
log Number of Clouds	**0.46/0.032**	**4.7/4.6 × 10^{-3}**
Net $\dot{M}$($M_\odot$ yr^{-1})	0.31/0.28	0.084/> 0.25
$L_{\rm KE}$ [erg s^{-1}]	0.42/0.10	1.4/0.09
$L_{\rm KE}/L_{\rm Bol}$	0.30/0.41	0.37/0.24
Predicted [O III] Luminosity	0.26/0.49	0.56/0.19
Covering-fraction Correction	**0.58/2.1 × 10^{-3}**	**9.3/< 0.001**

Notes.
[a] Kolmogorov–Smirnov two-sample test. Each entry has two numbers: the first is the value of the statistic, and the second is the probability p that the two samples arise from the same parent sample. Bold type indicates entries that yield $p < 0.05$.
[b] Anderson–Darling two-sample test. Each entry has two numbers: the first is the value of the statistic, and the second is the probability p that the two samples arise from the same parent sample. Note that the implementation used does not compute a probability larger than 0.25 or smaller than 0.001. Bold type indicates entries that yield $p < 0.05$.

log $\Delta R = -1.8$ pc, log volume filling fraction $= -3.8$, and log number of clouds $= -0.54$). The $E1 > 0$ objects have thinner outflows, smaller volume filling fractions, and more clouds are necessary to cover the continuum emission ($\Delta R = -2.4$ [pc], log volume filling fraction $= -5.6$, and log number of clouds $= 0.34$). These properties are discussed further in Section 4.3.2. The covering-fraction correction factor is lower for the $E1 < 0$ than for the $E1 > 0$ objects (median values of 0.6 and 1.5, respectively); this parameter was defined in Section 2.1 and is discussed in detail in Section 4.4.

The ionization parameter, log$a$, and the force multiplier show suggestions of differences. Specifically, while the highest ionization parameter represented by $E1 > 0$ objects is log $U = -0.5$, 25% of $E1 < 0$ objects have ionization parameters larger than that value (Figure 1). Likewise, lower values of the force multiplier are dominated by $E1 < 0$ objects (Figure 1). In addition, the kinetic luminosity $L_{\rm KE}$ and the ratio of the kinetic to bolometric luminosity are consistently lower for the $E1 < 0$ objects (Figure 1).

3.2. Correlations

In Leighly et al. (2022), we examined the relationships among the optical and derived parameters such as the bolometric luminosity. In this paper, we compare those parameters with the *SimBAL* parameters, both for the full sample, and for the sample segregated by the $E1$ parameter. We used the Spearman rank correlation for our comparisons.

We first correlated the *SimBAL* parameters with one another. A correlation analysis of the *SimBAL* results for the full 50 object sample is given in Section 6.1 of Choi et al. (2022). Here we considered only the low-redshift subsample. The results are shown in Figure 2. The plots represent the log of the p value for the correlation, where the sign of the value gives the sense of the correlation. That is, a large negative value implies a highly significant anticorrelation.

Parameter uncertainties were propagated through the correlations using a Monte Carlo scheme. We made 10,000 normally distributed draws of each parameter, where the distribution was stretched to the size of the error bar. Asymmetrical errors were accounted for by using a split-normal distribution (i.e., stretching the positive draws according to the positive error, and the negative draws according to the negative error). We chose $p < 0.05$ as our threshold for significance. In most cases, taking the errors into account did not dramatically change the significance of a correlation, if present.

There are several extremely strong correlations among the *SimBAL* parameters (Figure 2) that were also observed for the full sample Choi et al. (2022). As we discuss only FeLoBALQs in this paper, most gas columns extend beyond the hydrogen ionization front[12] in order to include sufficient Fe^+ ions to create an observable absorption line. The thickness of the H II region increases with the ionization parameter, a fact that explains the strong correlation between the column density and the ionization parameter. The net mass outflow rate is a function of the velocity, explaining the strong correlation between those two parameters. The force multiplier depends inversely on the ionization parameter.

We also correlated the *SimBAL* parameters for the $E1$-divided samples (Figure 2). As noted above, $E1$ is related to the Boroson & Green (1992) Eigenvector 1, which dominates the variance in quasar properties. The motivation for looking for correlations among the $E1$-divided samples is that by removing that dominant dependence, more subtle parameter dependencies may be revealed.

Finally, Figure 3 shows the correlations between the 17 optical and global parameters and the 18 *SimBAL* parameters. A special technique was used to handle these data because there are 30 objects and 36 outflow components. Five of the objects showed multiple outflow components[13]; Choi et al. (2022, Section 6.2) discussed the need for multiple outflow components in these objects. We assumed that physically one of the components is more representative than the other one or two. For example, [O III] may be produced by one component in the outflow but not another. Likewise, the outflow location may be correlated with the outflow velocity for components that share some fundamental property (i.e., perhaps they are the main outflow in the system), but other subsidiary outflows do not obey this trend. Therefore, we computed the correlations among all combinations and present the statistically most significant ones.

[12] The hydrogen ionization front is the location in a slab of photoionized gas where the hydrogen-ionizing photon flux is exhausted. In the context of H II regions, it is the location of the Strömgren sphere.
[13] SDSS J025858.17−002827.0, SDSS J103903.03+395445.8, SDSS J104459.60+365605.1, SDSS J112526.12+002901.3, and SDSS J144800.15+404311.7. SDSS J144800.15+404311.7 has three outflow components; the other objects have two.

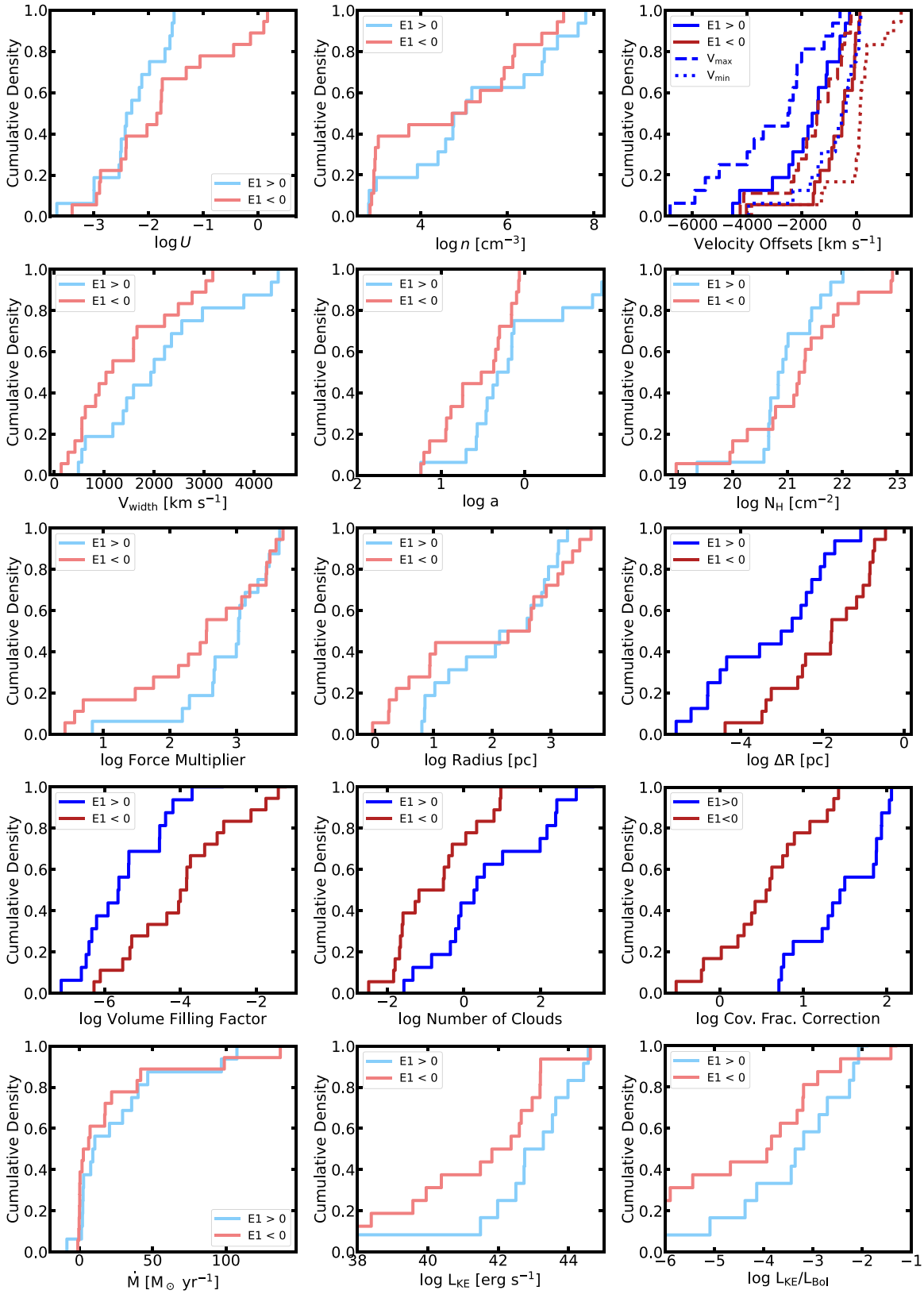

Figure 1. Cumulative distributions of 17 of the *SimBAL* parameters segregated by their $E1$ parameter values. Distributions that are significantly different ($p < 0.05$; Table 1) are shown in dark red and dark blue, while distributions that are not significantly different are shown in a pale hue of the same color. All of the outflow velocity parameters (V_{off}, V_{max}, V_{min}) are shown in the top-right panel. Of the *SimBAL*-related parameters, those three, the thickness of the absorber, the log filling factor, the number of clouds covering the continuum-emission-line region, and the covering-fraction correction (discussed in Section 4.4) show statistically different distributions between the $E1 > 0$ and $E1 < 0$ subsets.

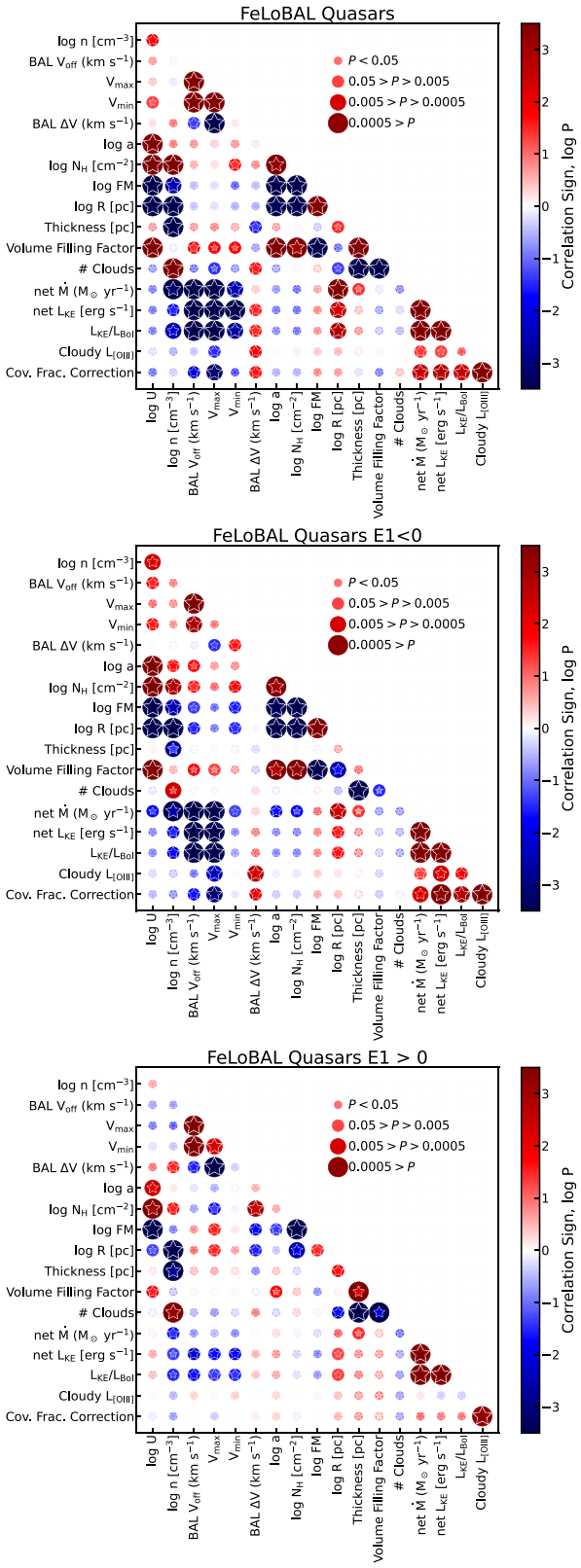

Figure 2. Results of the Spearman rank correlation analysis for the 18 *SimBAL* parameters. The stars show the results for a Monte Carlo scheme to estimate the effects of the errors; see Leighly et al. (2022) for details. The top plot shows the results for the whole sample, while the middle and bottom plots show the results divided by the $E1$ parameter. Of particular interest is the weak but significant anticorrelation between the velocity parameters and location of the outflow for $E1 < 0$ and the correlation for the same parameters for $E1 > 0$.

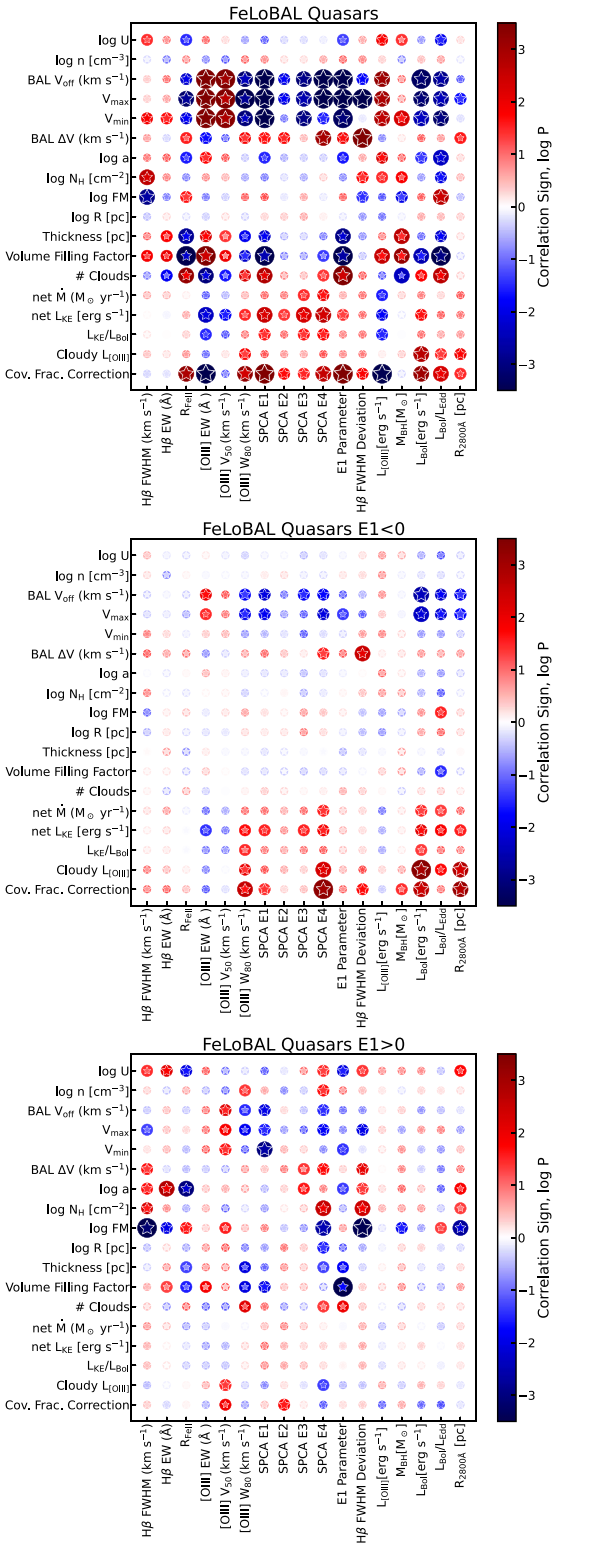

Figure 3. Results of the Spearman rank correlation analysis for the 17 optical emission-line parameters and global properties and the 18 *SimBAL* absorption-line and derived properties. The symbols have the same meaning as in Figure 2. The top plot shows the results for the 30 object low-redshift sample, while the middle and bottom plots show the results for the $E1 < 0$ and $E1 > 0$ subsamples, respectively. Among the optical parameters, $E1$ and the related parameters $R_{\rm FeII}$, [O III] equivalent width, SPCA1, $E1$, $L_{\rm Bol}$, and $L_{\rm Bol}/L_{\rm Edd}$, are most strongly correlated with the *SimBAL* parameters. Among the *SimBAL* parameters, the offset velocities and parameters associated with the volume filling fraction are the most strongly correlated with the optical parameters.

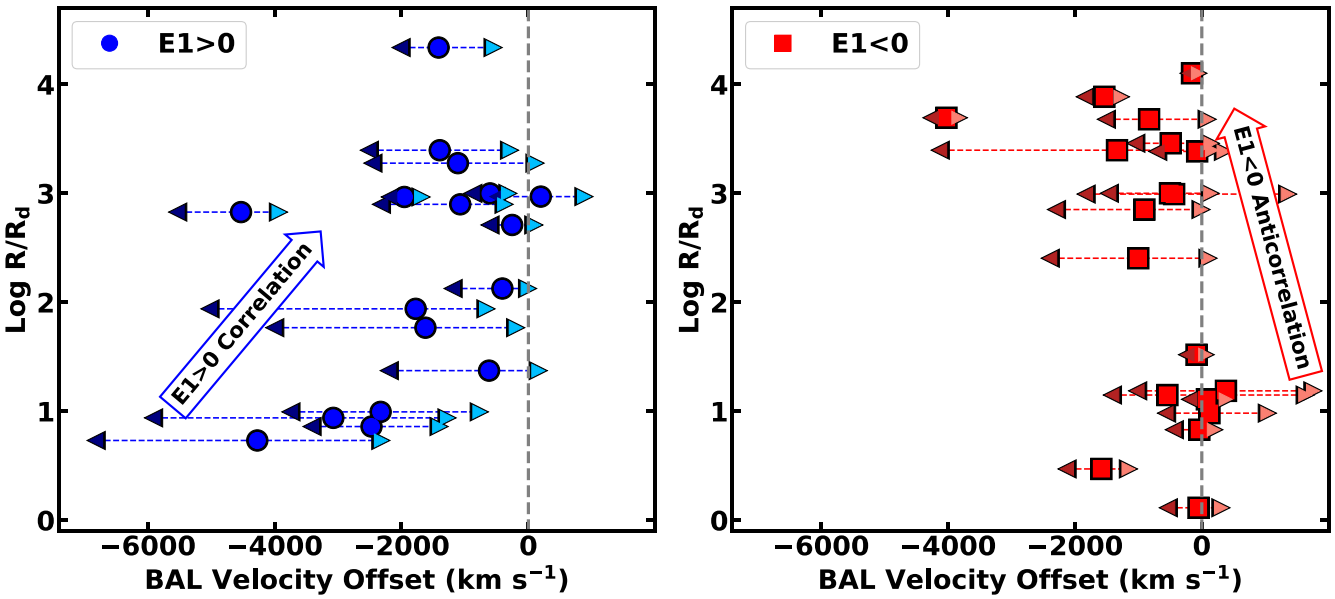

Figure 4. Location of the outflow determined using *SimBAL* modeling (Choi et al. 2022) and normalized by the dust sublimation radius as a function of the outflow velocity. Negative velocities denote outflows. The circles and squares show the column-density-weighted velocity, while the left and right triangles show the maximum and minimum speeds, respectively. There is an anticorrelation (correlation) between $\log R/R_{\rm d}$ and the outflow velocity for the $E1 < 0$ ($E1 > 0$) FeLoBALQs. These different behaviors imply a difference in the formation and acceleration of outflows for the two classes of FeLoBALQs.

4. Analysis

4.1. The Location of the Outflow

An interesting set of patterns observed among the *SimBAL* parameters is shown in Figure 4. We plot the velocity of the outflow as a function of the log of the radius divided by the dust sublimation radius ($R_d = 0.16L_{45}^{1/2}$ pc; Elitzur & Netzer 2016); note that $R_{\rm d}$ is close to 1 pc in these samples. It is immediately apparent that among the compact outflows $\log R/R_d < \sim 2$, the $E1 > 0$ objects have systematically larger velocity outflows than the $E1 < 0$ objects.

While there is no correlation between the location of the outflow $\log R/R_{\rm d}$ and the outflow velocity for the sample as a whole, we found a tentative or marginal correlation for the $E1 > 0$ subsample and an anticorrelation for the $E1 < 0$ subsample (p values are reported later in the text). $E1 < 0$ objects with outflows close to the central engine generally have no net outflow velocity, while those located far from the central engine show modest outflows. In contrast, some of the largest velocities in the sample are found in $E1 > 0$ object outflows located close to the central engine, while at larger distances, the velocities tend to be lower.

The correlation between the outflow velocity and $\log R/R_{\rm d}$ observed among the $E1 > 0$ objects might be expected from a high-accretion-rate quasar. The terminal velocity for a radiatively driven outflow is larger at smaller radii because of the higher available photon momentum, which means that larger velocity at small radii would be needed for a sustained (i.e., not failed) wind.

Choi et al. (2022) identified a new class of FeLoBALQs called "loitering" outflows as objects that have $\log R < 1$ [pc] and a velocity offset of the excited-state Fe II λ2757 of $|v_{\rm off}|_{\rm FeII\ excited} < 2000$ km s^{-1} (Figure 18 of Choi et al. 2022). They found that the loitering outflow objects had distinct photoionization properties too: they have larger ionization parameters and densities compared with the full sample. Leighly et al. (2022) found that, in the low-redshift subsample, almost all loitering outflow objects had $E1 < 0$ and were therefore categorized as low-accretion-rate objects.

We next try to understand the origin of the low velocities among the loitering outflows. The high ionization parameter ($-2 < \log U < 0.5$; Figure 6 of Choi et al. 2022) and accompanying large column density ($\log N_H > 21.5$ (cm^{-2}); Figure 7 of Choi et al. 2022) yield a low force multiplier; basically, the slab has very large column of gas where the illuminated face and a significant fraction of the total column density are too ionized to contribute much to resonance scattering (e.g., Arav et al. 1994). The $E1 < 0$ objects are characterized by a low Eddington ratio ($\log L_{\rm Bol}/L_{\rm Edd} < -0.5$), which means that the radiative flux is small relative to the gravitational binding of the black hole and therefore it is less able to accelerate the outflow gas. Thus, the combination of the large outflow column and low radiative flux compared with gravity may explain the low velocities ($V_{\rm off} < -2000$ km s^{-1}; Figure 18 of Choi et al. 2022).

However, not all $E1 < 0$ objects have loitering outflows; at larger radii, near $\log R/R_{\rm d} = 3$, the $E1 < 0$ objects merge with the $E1 > 0$ objects, and outflows of both $E1$ groups have velocities near -1000 km s^{-1}. The combination of near-zero velocity for small $\log R/R_{\rm d} < 2$ and outflows for larger $\log R/R_{\rm d} > 2$ results in the anticorrelation between the outflow velocity and $\log R/R_{\rm d}$ among the $E1 < 0$ objects shown in Figure 4.

As seen in Figure 1, it is clear that the $E1 > 0$ objects have systematically larger velocity outflows than the $E1 < 0$ objects; the probability that they are drawn from the same population is less than 1.6% (Table 1). However, correlations between the outflow velocity and the location of the outflow are barely or arguably not significant, and might be construed to fall in the realm of p hacking. For example, if we examine $\log R$ as a function of $V_{\rm off}$, then the $E1 < 0$ correlation is significant ($p = 0.025$) but the $E1 > 0$ is not ($p = 0.076$), while for $\log R/R_d$, the $E1 < 0$ correlation is not significant ($p = 0.052$) while $E1 > 0$ is significant ($p = 0.050$). On the other hand,

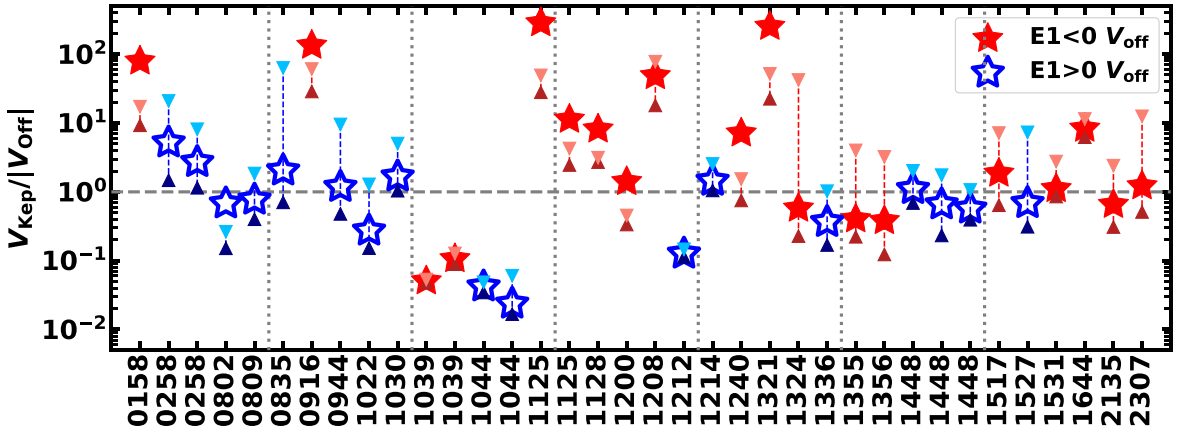

Figure 5. Ratio of the Keplerian velocity at the location of the outflow to the absolute value of the outflow velocities. The stars denote V_{off}. The triangles show V_{min} and V_{max} and can be offset from the stars if the trough includes both inflow and outflow. Very large values of this ratio show absorption features that have velocities much lower than the Keplerian velocity.

these correlations are principally driven by the differences in the velocity distributions at $\log R < 2$ [pc], which are very clear from Figure 4. Regardless, these differences in the behavior of the outflow velocity among the $E1 < 0$ and $E1 > 0$ objects may point to a difference in formation and acceleration of outflows among those two classes of objects. In particular, if the $E1$ parameter is considered to be a proxy for L_{Bol}/L_{Edd}, these differing behaviors may point to a difference in the formation and acceleration of outflows as a function of that parameter. The relationship between potential acceleration mechanisms and the origin and location of FeLoBAL winds is discussed extensively in Choi et al. (2022) Section 7.2.

Using the black hole masses estimated in Leighly et al. (2022) we computed the Keplerian velocities at the location of the outflow. We then computed the ratio of the Keplerian velocity to the outflow velocity V_{off}, as well as the ratio to V_{min} and V_{max}, and plot the results in Figure 5. This plot shows several interesting features. Large values of $V_{Kep}/|V_{off}|$ indicate absorption features that have line-of-sight velocities much lower than the local Keplerian velocity (e.g., SDSS J1125 +0029, SDSS J1321+5617). A number of $E1 < 0$ objects fall into this category. Because the continuum-emission region is so small compared with the outflow location (Section 4.3), this phenomenon could be achieved if the outflow velocity vector lies strictly along the line of sight to the nucleus, and the local Keplerian motion is principally tangential.

On the other hand, very low values of $V_{Kep}/|V_{off}|$ indicate objects with outflow velocities very much larger than the local Keplerian velocity (e.g., SDSS J1039+3954, SDSS J1044 +3656). Small values suggest that the outflow is kinematically decoupled from the gravitational potential of the black hole. It is possible that these small ratios signal a distinct acceleration mechanism for their outflows, such as the "cloud-crushing" mechanism suggested by Faucher-Giguère et al. (2012), rather than radiative line driving or dust acceleration, where the magnitude of those mechanisms scales with the location of the outflow.

Finally, a number of the outflows show $V_{Kep}/|V_{off}|$ commensurate with unity. Most of the $E1 > 0$ objects fall into this category. Of particular interest is SDSS J1448+4043. Choi et al. (2022) found that the *SimBAL* solution required three separate outflow components in this object (Section 6.2 of that paper). The lowest velocity component could be seen to be kinematically distinct, as it is narrow and shows a prominent ground-state Mg I λ2853 line. The other two features are kinematically blended in this overlapping trough object and were inferred to be distinct based on their photoionization properties (Figure 11 of Choi et al. 2022). They found that the outflows lie at dramatically different distances ($\log R =$ 0.84, 2.05, and >3.1 [pc]); yet their outflow velocities are commensurate with Keplerian velocity at those locations. These outflows could be considered kinematically coupled in some way to the gravitational potential of the black hole.

4.2. Bolometric Luminosity

The plot illustrating the results of the correlation analysis (Figure 3) reveals the most frequently observed relationship among BAL quasar outflows: the correlation of the luminosity and Eddington ratio with the outflow speed ($p = 5 \times 10^{-4}$ and $p = 1.2 \times 10^{-3}$, respectively). The relationship between the BAL outflow velocity and Eddington ratio is shown in Figure 6. These relationships have been previously reported for HiBALQs (Laor & Brandt 2002; Ganguly et al. 2007; Gibson et al. 2009) and are generally found among objects with outflows (e.g., Fiore et al. 2017). Ganguly et al. (2007) noted that the terminal velocity of an outflow should scale with the Eddington ratio as $v_{terminal} \propto (L_{bol}/L_{Edd})^{1/2}$ (Hamann 1998; Misawa et al. 2007); this dependence arises from the solution of the conservation of momentum equation (e.g., Leighly et al. 2009) assuming that the outflow is accelerated by radiation. Thus the outflow velocity is predicted to be correlated with the luminosity relative to the Eddington value. However, a linear relationship between these two quantities is not what is observed; rather, there is usually an upper-limit envelope of velocity as a function of the luminosity or L_{bol}/L_{Edd}. That is, at any luminosity, there is a range of outflow velocities up to some upper-limit value, and those upper-limit values are correlated with the luminosity. For example, see Figure 6 in Laor & Brandt (2002) and Figures 6 and 7 in Ganguly et al. (2007). This upper-limit relationship is seen in our data too (Figure 6, top).

Theoretically, the speed of a radiatively driven outflow should also depend on two factors: 1) the launch radius (because the flux density of the radiation drops as R^{-2}) and 2) the force multiplier (because the ability of an outflow to use the photon momentum depends on which ions that can scatter the photons are available). Using the momentum conservation

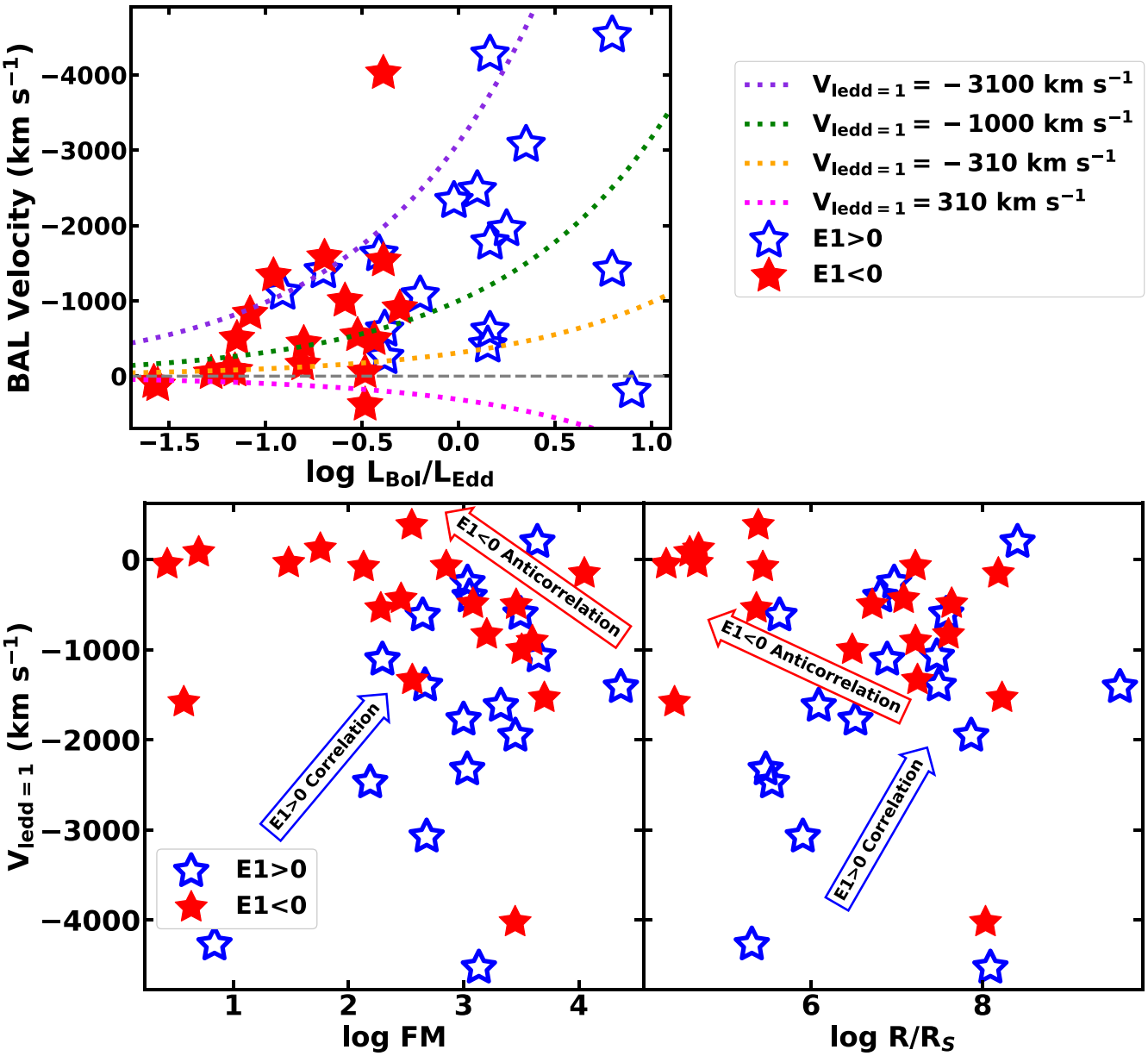

Figure 6. BAL outflow velocity as a function of the Eddington ratio for the sample of low-redshift FeLoBALQs. *Top:* The sample shows the $V \propto L_{\rm bol}/L_{\rm Edd}$ upper-limit envelope behavior commonly found in BALQs (Laor & Brandt 2002; Ganguly et al. 2007); see text for details. The scatter below the envelope can be characterized by parameter $V_{\rm ledd=1}$, the velocity any object would have if $L_{\rm bol}/L_{\rm Edd} = 1$ (see text for details). *Bottom left:* An anticorrelation between the force multiplier and $V_{\rm ledd=1}$ indicates that the scatter in the $E1 < 0$ objects may be caused by the scatter in *FM*. *Bottom right:* A correlation of R/R_S with $V_{\rm ledd=1}$ suggests that the scatter in the $E1 > 0$ objects may be caused by the scatter in R/R_S.

equation it can be shown that

$$v \sim FM^{1/2}(L/L_{\rm Edd})^{1/2}(R_{\rm launch}/R_{\rm S})^{-1/2},$$

where $R_{\rm S}$ is the Schwarzschild radius. The launch radius is difficult to determine, but we can estimate it by assuming that the measured velocity is some representative fraction of the terminal velocity. For a β velocity law[14], the launch radius is a constant fraction of the radius at which the outflow is observed, i.e., $R_{\rm launch}/R_{\rm S} \approx R/R_{\rm S}$. While this approximation would be inadequate to solve an equation of motion for a single object (e.g., Choi et al. 2020), it may be sufficient to compare a sample of objects. The force multiplier, defined to be the ratio of the total opacity to the electron scattering opacity, is an output of *Cloudy*; it includes both line and continuum opacity.

Armed with these relationships and approximation, we can investigate whether the scatter in the outflow velocity for a given $L_{\rm bol}/L_{\rm Edd}$ could be a consequence of intrinsic scatter, whether there are trends in either the launch radius or the force multiplier, or whether both cases may apply. To put it another way, if the velocity upper-limit envelope describes the behavior of an optimal outflow, perhaps the objects below that optimal level may be deficient in either their force multiplier or their launch radius.

We note that there is another factor that could be important: the angle of the line of sight to the velocity vector. We do not discuss that factor here, which means that there should be

[14] A β velocity law is expressed as $v(r) = v_\infty(1 - R_{\rm Launch}/r)^\beta$ where v_∞ is the terminal velocity, and $R_{\rm Launch}$ is the launch radius. It is often used for modeling winds from hot stars.

additional intrinsic scatter associated with that parameter. In addition, dust scattering may be important in accelerating quasar outflows (e.g., Thompson et al. 2015; Ishibashi et al. 2017), and our use of the force multiplier means that we are only considered continuum and resonance scattering for the acceleration mechanism. Additional discussion of the potential role of dust scattering in acceleration in FeLoBALQ outflows can be found in Choi et al. (2022) Section 7.2.

We investigated these questions by first defining a parameter $V_{\rm ledd=1}$ that describes how far below the optimal outflow velocity an object lies on the Eddington ratio versus the velocity as shown in Figure 6. That is, we solved $V_{\rm off} = V_{\rm ledd=1}(L_{\rm bol}/L_{\rm Edd})^{1/2}$ for $V_{\rm ledd=1}$, where $V_{\rm off}$ is plotted as the y axis in the top panel of Figure 6. Then, for any particular object, $V_{\rm ledd=1}$ is the velocity that it would have if $L_{\rm bol}/L_{\rm Edd} = 1$. In essence, we have derived a parameter that can be used to compare objects as though they have the same $L_{\rm bol}/L_{\rm Edd}$ (similar to the concept of the absolute magnitude). Traces for representative values of $V_{\rm ledd=1}$ are shown in Figure 6. We then plotted this parameter against the force multiplier and R/R_S (Figure 6).

We first considered the force multiplier. We found that the force multiplier is not correlated with $V_{\rm ledd=1}$ for the whole sample, but it is marginally anticorrelated for the $EI < 0$ objects ($r_s = -0.46$, $p = 0.047$), and correlated for the $EI > 0$ objects ($r_s = 0.62$, $p = 6.7 \times 10^{-3}$). Keeping in mind that $V_{\rm ledd=1}$ is negative for outflows, this means that $EI < 0$ objects with larger FM have higher outflow velocities. We interpret this behavior to mean that unfavorable FM (too small) is responsible for nonoptimal (i.e., below the envelope) outflows in the $EI < 0$ objects. In contrast, the correlation for the $EI > 0$ objects means that the $EI > 0$ objects with low FM have higher outflow velocities, opposite of the physical expectation. We interpret this to mean that $EI > 0$ objects produce their outflows *despite* nonoptimal FM values, and therefore another factor is causing the below-envelope scatter in the $EI > 0$ objects.

Turning to R/R_S, we found that, while there is no correlation between this parameter and $V_{\rm ledd=1}$ for the sample as a whole, there is an anticorrelation for the $EI < 0$ objects ($r_s = -0.52$, $p = 0.023$) and a correlation for the $EI > 0$ objects ($r_s = 0.51$, $p = 0.035$). Again keeping in mind that $V_{\rm ledd=1}$ is negative for outflows, the correlation between R/R_S and $V_{\rm ledd=1}$ means that objects with smaller R/R_S have larger outflow speeds, as predicted by the solution to the momentum conservation equation above. This correlation suggests that the below-envelope scatter among the $EI > 0$ objects is caused by unfavorable (too large) R/R_S (Figure 6, bottom panel). The anticorrelation seen among the $EI < 0$ objects can be interpreted as implying that R/R_S is less important in determining their outflow velocity.

Finally, we can compare the $V_{\rm ledd=1}$ values for the $EI < 0$ and the $EI > 0$ objects. It turns out that the $V_{\rm ledd=1}$ distributions for the two classes are statistically indistinguishable. That is, both types of objects lie along the same set of $V_{\rm ledd=1}$ traces in Figure 6. The $EI < 0$ objects have both systematically lower outflow velocities (Figure 1) and systematically lower $L_{\rm bol}/L_{\rm Edd}$ (Figure 7, Leighly et al. 2022). This result implies that $EI > 0$ objects reach a larger velocity because of their larger $L_{\rm bol}/L_{\rm Edd}$, i.e., $L_{\rm bol}/L_{\rm Edd}$ is primary for both classes of objects.

We have shown that in the low-redshift subsample of FeLoBALQs the outflow velocity depends on $L_{\rm bol}/L_{\rm Edd}$. This is not a new result; it has been seen before in other samples (e.g., Ganguly et al. 2007). Such a result is relatively simple to extract from any set of BAL quasars, depending as it does only on estimation of the outflow velocity (e.g., from the C IV trough) and an estimate of the Eddington luminosity. That requires an estimate of the black hole mass, which is arguably most reliably extracted from Hβ but can also be estimated using Mg II and C IV, in principal, although difficult in FeLoBALQs due to the heavy absorption. The difference in our analysis is that, because *SimBAL* yields the physical conditions of the outflow (including $\log U$, $\log n$, $\log N_H$), we can investigate this relationship in more detail and parse the dependence on the subsidiary parameters: the force multiplier and the estimated launch radius. We discovered a difference in the velocity dependence of these two parameters among the two accretion classes. So while $L_{\rm bol}/L_{\rm Edd}$ is principally responsible for determining the outflow velocity, the force multiplier (launch radius) is responsible for producing the scatter in the velocity at a particular value of $L_{\rm bol}/L_{\rm Edd}$ in the $EI < 0$ ($EI > 0$) objects. This result provides additional evidence for differences in the acceleration mechanism.

4.3. Geometry Properties of the Outflow

4.3.1. The Full Sample

The volume filling factor ($\Delta R/R$, $\Delta R = N_H/n_H$) gives us information about the physical size scales of the outflowing gas. It is most directly interpreted as the fractional volume of space occupied by the outflow. Typically, using the values for the column density, density, and radius derived using excited-state absorption lines, small log volume filling factors, mostly ranging between -6 and -4 are found (e.g., Korista et al. 2008; Moe et al. 2009; Dunn et al. 2010). The volume occupied by the absorbing clouds ranges from 0.01% to 1%. The volume filling factor tells us how thin or extended in the radial direction the BAL cloud structure is and provides us with information about the BAL physical conditions. A small volume filling factor ($\log \Delta R/R \sim -5$) for BALs may imply a pancake- or shell-like geometry that is very thin in the radial direction (e.g., Gabel et al. 2006; Hamann et al. 2011, 2013). These BAL absorbers with $\log \Delta R/R \lesssim -3$ may be composed of smaller gas clouds (e.g., Waters & Proga 2019) that are potentially supported by magnetic confinement in order to avoid dissipation (e.g., de Kool & Begelman 1995). In contrast, Murray & Chiang (1997) proposed that a continuous flow from the accretion disk is the origin of broad emission lines and BAL features; such a flow would have a volume filling factor of 1. We emphasize that our results are not consistent with a direct observation of a disk wind because the size scales that we measure are too large. The minimum distance of the outflow from the central engine found in our sample is $R \sim 1$ pc in SDSS J1125+0029, whereas reasonable size scales for disk wind outflows should be comparable to the size of the accretion disk ($R \ll 0.01$ pc). That does not imply that disk winds do not exist but rather that we do not find them to have rest-UV BAL outflow signatures. This result is consistent with the literature; among the FeLoBALQs previously subjected to detailed analysis, typical outflow distances lie between 0.4 and 700 pc (e.g., de Kool et al. 2001, 2002a, 2002b; Moe et al. 2009; Dunn et al. 2010; Aoki et al. 2011; Lucy et al. 2014; Shi et al. 2016;

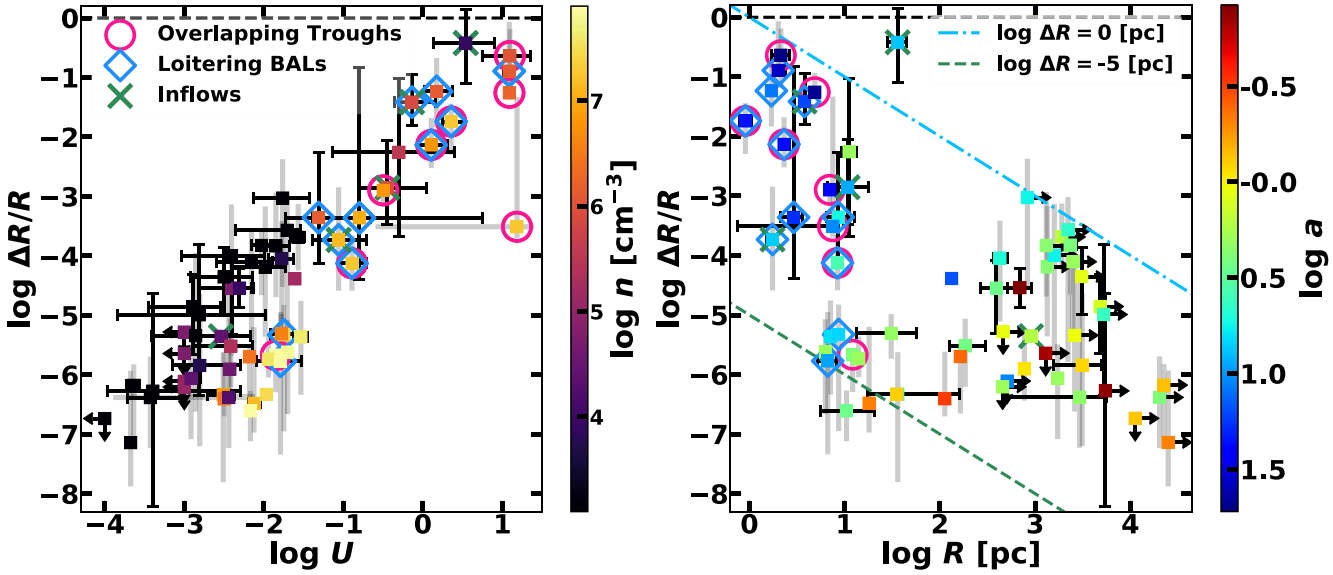

Figure 7. Volume filling factor ($\log \Delta R/R$) as a function of the ionization parameter ($\log U$) and the location of the outflow ($\log R$). We found a wide range of $\log \Delta R/R$, with the overlapping trough and loitering BALs having higher values of $\log \Delta R/R$. *Left panel*: $\log \Delta R/R$ increases with $\log U$ following the slope of ∼1.5. This tight correlation is expected given the relationship between $\log U$ and $\log N_H$ for FeLoBALs (Section 5.3, Choi et al. 2022). One of the main sources of the scatter along the $\log \Delta R/R$ can be ascribed to the range of $\log n$ observed in the sample. *Right panel*: We found a wider range of $\log \Delta R/R$ distribution for the FeLoBALs that are located close to the central black holes. The green (dashed) and blue (dotted–dashed) diagonal lines represent the locations of the constant physical thickness of the BAL winds at $\log \Delta R = -5$ and 0 [pc], respectively. The error bars show 2σ uncertainties, and the gray shaded bars represent the range of the values among the tophat model bins for each BAL.

Hamann et al. 2019; Choi et al. 2020), i.e., no closer than the broad-line region.

We calculated the volume filling factors for the full sample and examined the dependence on BAL properties (Figure 7). The strong correlation seen between $\log \Delta R/R$ and $\log U$ can be explained by the mathematical relationship between the parameters as follows. First, the BAL physical thickness (ΔR) is proportional to the hydrogen column density (N_H), which is also proportional to the ionization parameter U as $\log N_H - \log U$ is nearly constant in the FeLoBALQ sample, and the distance of the outflow from the central SMBH (R) is inversely proportional to $U^{1/2}$, both for a fixed density. Dividing the BAL thickness by its distance from the center, we obtain the volume filling factor $\Delta R/R \propto U^{1.5}$, and we find a slope of ∼1.5 in the left panel of Figure 7. We observe a scatter around that line because of the range of $\log N_H - \log U$ and $\log n$ for the FeLoBALs in our sample (Figure 4, Choi et al. 2022). There is also a range in photoionizing flux Q, which we assume to be proportional to $L_{\rm Bol}$. This parameter enters through $U = Q/4\pi R^2 nc$. Therefore, larger values of $\log N_H - \log U$ (thicker outflows), smaller density, or smaller $\log L_{\rm bol}$ correspond to a larger value of $\log \Delta R/R$.

The distribution of $\log \Delta R/R$ is not uniform across $\log R$. At large radii, corresponding to $\log U \lesssim -1$, the volume filling factors mostly range between −6 to −4. These values are similar to those reported in the literature for samples of high-ionization BAL quasars (e.g., Gabel et al. 2006; Hamann et al. 2011, 2013). In contrast, the outflows that are found at $\log R \lesssim 1$ have a very wide range of $\log \Delta R/R$, ranging from −6 to nearly almost zero. These are mostly the special types of BALs that were identified in Choi et al. (2022), including the overlapping trough and loitering BALs.

The analysis for the full sample shows significant differences in $\log \Delta R/R$ as a function of radius. This result suggests that BAL winds may favor different models at different radii (Choi et al. 2022; K. M. Leighly et al. 2022, in preparation). The compact winds at $\log R \lesssim 1$ [pc] showed a wide range of $\log \Delta R/R$ that agrees with the predictions of the various BAL physical models that explain either thin shell-like outflows (small volume filling factor) or stream-like outflows (large volume filling factor). On the other hand, the properties of distant BAL winds only favor the physical model with a thin pancake-like BAL geometry. Specifically, Faucher-Giguère et al. (2012) proposed that FeLoBALs with large $\log R \gtrsim 3$ [pc] and small $\log \Delta R/R \sim -5$ are formed by "cloud crushing" where the ambient ISM is shocked by the supersonic energy-conserving quasar outflow and FeLoBALs are formed in situ at kiloparsec scales rather than formed near the accretion disk. In addition, in order for distant BALs to have large filling factors, the BAL clouds would need to have large physical radial thicknesses proportional to their distances from the central engine ($\Delta R \gtrsim 10$ pc). Maintaining such a large structure is physically challenging due to cloud destructive processes (e.g., Proga & Waters 2015).

4.3.2. The z < 1 FeLoBALQs and the E1 Dependence

In this section, we discuss the relationship between the BAL outflow parameters involving the geometry of the outflow and the optical-band emission-line properties. We have emission-line properties only for the 30 object $z < 1$ subsample, so this discussion only involves that subsample. In particular, we investigated how the parameters that describe the geometrical properties of the outflow depend on the $E1$ parameter and, by extension, the accretion rate.

We first investigated the physical thickness of the gas ΔR. We showed in Section 3.1 that the ΔR parameter is significantly different for the $E1 < 0$ and $E1 > 0$ subsamples (Figure 1 and Table 1); the median log thickness is about 1 dex larger for the $E1 < 0$ objects. This result arises because although there is no statistical difference in $\log U$ between the $E1 < 0$ and $E1 > 0$, there is a tendency for $E1 < 0$ objects to

have larger log$U$ and therefore thicker outflows. The thickness is also anticorrelated with both $R_{\rm FeII}$ and the $E1$ parameter (Figure 3) for the same reason.

We next considered the volume filling factor for the low-redshift subsample. We found that $E1 < 0$ objects have significantly larger volume filling factors than $E1 > 0$ objects because of the significant difference in thickness log ΔR but also that $E1 < 0$ objects tend to have larger log$U$ and therefore smaller log$R$, i.e., to be located closer to the central engine.

Because we have black hole mass and accretion rate estimates (Leighly et al. 2022), we can estimate the number of spherical clouds required to completely cover the continuum-emission region. This parameter is useful to visualize the BAL absorption region in the quasar. The first ingredient in this computation is the size of the emission region R_{2800}. We calculated the size of the 2800 Å continuum-emission region using the procedure described in Section 6.1 of Leighly et al. (2019b). To summarize, we used a simple sum-of-blackbodies accretion disk model (Frank et al. 2002) and assigned the 2800 Å radius to be the location where the radially weighted brightness dropped by a factor of e from the peak value. Among the objects in this sample, this parameter spans a rather small range of values with 90% of the objects having $-2.9 < \log R_{2800} < -2.3$ [pc] (Figure 8, Leighly et al. 2022). This is likely a consequence of the T^4 dependence of the accretion disk.

The second consideration is the wide range of angular diameters that the continuum-emission region will subtend at the location of the outflows. For example, the continuum-emission region will subtend an angular diameter that is 1000 times larger to a wind located at 1 pc than to one located at 1000 pc. Folding in the small difference in size of the continuum-emission region we found that the largest angular diameter is presented to the higher-velocity component of SDSS J1125+0029 at 18 arcmin[15], and the smallest is the higher-velocity component of SDSS J1044+3656 at 4.5×10^{-4} arcmin.

The final ingredient is the transverse size of the absorber. This parameter cannot be measured directly from these data as absorption is a line-of-sight measurement. Instead, we make the simplifying order-of-magnitude assumption that the absorbing gas occurs in clouds, and the clouds are approximately spherical. Making this assumption yields a transverse size that is equal to ΔR, the thickness of the absorbing gas.

Employing these three ingredients (the size of the continuum-emission region R_{2800}, the angular diameter that the continuum-emission region will subtend at the location of the outflow, and the transverse size of the absorbing cloud), we can determine the number of clouds required to cover the continuum-emission region. For example, if the angular size of the cloud from the perspective of an observer located at the continuum-emission region is the same as the angular size of the continuum-emission region at the location of the cloud, then only one cloud is required to cover the continuum-emission region.[16] Conversely, if the angular size of the cloud from the perspective of an observer located at the continuum-emission region is much smaller than the angular size of the continuum-emission region from the perspective of a viewer located at the outflow, then many clouds are required. The number of clouds is the ratio of the area of the continuum-emission region and the transverse area of the cloud. For this order-of-magnitude computation, we assume that the continuum-emission region is viewed face on.

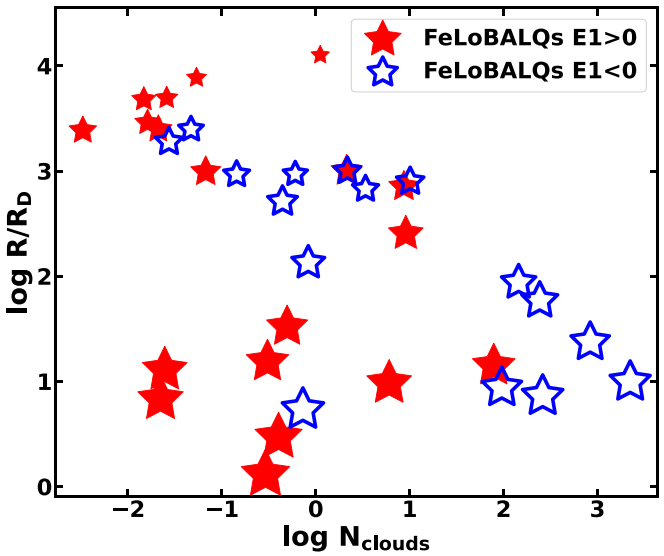

Figure 8. Relationship between the number of clouds required to occult the 2800 Å continuum emission region and the location of the outflow normalized by the dust sublimation radius. The size of the points is scaled with the angle subtended by the continuum emission region as viewed from the location of the outflow. Compact outflows (those with $\log R/R_{\rm D} < 2$) are segregated by the $E1$ parameter, with $E1 < 0$ objects having macroscopic clouds and $E1 > 0$ objects requiring 100–1000 s of cloudlets to cover the source.

The resulting number of clouds spans a huge range for the sample. Ninety percent of the values fall between 0.016 (which means that the inferred size of the cloud is about 60 times larger than the emission region) to ∼1000, a factor of more than 60,000. Moreover, there is a significant difference between $E1 < 0$ and $E1 > 0$ objects (Figure 1; Table 1); the median values of the log of the number of clouds are 0.3 and 2.2, respectively.

The $E1 > 0$ outflows located close to the central engine (lower right in Figure 8) require a large number of clouds (100–1000 s) to cover the continuum-emission region. Their outflows are characterized by a lower ionization parameter (typically less than −1.5) compared with the $E1 < 0$ objects ($\log U \sim 0$), and therefore the physical thickness of the outflow is smaller in these objects. Physically, this scenario suggests that the outflow is a fine mist of cloudlets.

Objects in which the number of clouds is less than 1 are split between those at large distances from the central engine ($\log R/R_{\rm D} > 2$) and those at small distances ($\log R/R_{\rm D} < 2$). In these objects, the angular size of the BAL cloud structure is comparable or larger than the projected angular size of the continuum emission region. One possibility is that our simplifying estimate that the clouds are approximately spherical is wrong. For example, the number of clouds required to cover the continuum emission region could be much larger if each cloud were long and needle-like, with the long axis pointed toward the central engine. This scenario might be somewhat reasonable physically if the clouds are confined magnetically along field lines that are bent radially by radiation

[15] For reference, the angular diameter of the full moon is 31 arcmin.

[16] We note in passing that this is the same concept that is applied to the measurement of the size of the quasar continuum-emission region using gravitational microlensing. The gravitational lens caustics of a single star are very small, but if the continuum-emission region has a commensurate angular size (because the star is located in the quasar host galaxy), its light can be differentially magnified.

pressure (e.g., de Kool & Begelman 1995) or sheared by radiation pressure.

Another possibility is that the nature of the partial covering is different in some of the objects. The *SimBAL* model includes a power-law partial covering parameter log$a$ that may parameterize a mist of clouds uniformly covering the continuum emission region (see Leighly et al. 2019b, and references therein for discussion and visualization). The presence of power-law partial covering does not preclude the presence of step-function partial covering as well. The step-function partial covering can be understood as a partial occultation of the continuum emission region. There is some evidence for the presence of step-function partial covering in objects lying in the lower left corner of Figure 8. In several of these objects, the *SimBAL* models required that a portion of the continuum and/or emission lines be unabsorbed by the outflow (Section 6.4, Figure 17 Choi et al. 2022). Physically, this result might be expected when the continuum emission region has a large angular size from the perspective of the absorber, i.e., an absorber with small $\log R/R_{\rm d}$. It may mean that the outflow is not a mist of clouds uniformly covering the source, but a distribution of nearly continuous gas.

4.4. [O III] Emission from the BAL Gas

Outflows in quasars are also seen in ionized emission lines. For example, kiloparsec-scale outflows observed in emission lines such as [O III] are known to be common among luminous active galactic nuclei (e.g., Harrison et al. 2014; Bischetti et al. 2017; Vayner et al. 2021). More compact ionized emission-line outflows have been resolved in nearby objects; for example, ionized gas outflows have been found 0.1–3 kpc from the nucleus (Revalski et al. 2021). It is possible that ionized emission-line outflows and BAL outflows are related. The outflowing broad-absorption-line gas is photoionized, and therefore it must produce line emission. In particular, [O III] λ5007 line emission is an important coolant in photoionized gas (e.g., Osterbrock & Ferland 2006). It is possible that in some objects the same gas produces absorption lines along the line of sight as well as emission lines from all lines of sight.

There are several fundamental problems that make finding a connection difficult. While absorption is a line-of-sight effect, an emission line is an aggregate of many lines of sight, so that emission from gas not associated with the BAL would be included in any observed line emission. In other words, the covering fraction of the emitting gas needs not be the same as that of the absorbing gas. [O III] emission is observed to have a very large range of equivalent widths (6–84 Å; Shen et al. 2011) potentially originating in a range of gas covering fractions (Baskin & Laor 2005; Ludwig et al. 2009; Stern & Laor 2012). Moreover, line emissivity depends on density squared below the critical density, i.e., $n_{cr} = 6.8 \times 10^5\,{\rm cm}^{-2}$ for [O III] λ5007] (Osterbrock & Ferland 2006) and on the density above the critical density. Thus, the line emission might not be seen against the continuum if the density is too low. Finally, if the absorption lines are broad, then the line emission may be distributed over a large range of velocities, and the line may be too broad to be seen against the continuum.

We do not have information about the extent of the line emission for our objects. However, it is interesting to see if there is a correspondence or relationship between the predicted [O III] emission from the BAL gas and the observed [O III] emission. Xu et al. (2020) tackled this problem using a sample of seven $z \sim 2$ quasars. Those objects were chosen to have r-band magnitudes $\lesssim 18.8$ and deep Si IV $\lambda\lambda$1393.76, 1402.77 troughs. They found evidence for a link between the [O III] emission and the BAL absorption. However, they presented a conceptual error: they suggested that [O III] emission is suppressed at high densities. In fact, [O III] emission always increases with density. Rather than a decrease or suppression of [O III] at high densities, the property that decreases is the ratio of the [O III] emission with respect to lines with higher critical densities. This physics is the basis of the Si III]λ1893/C III] λ1909 density diagnostic used in the near-UV (e.g., Leighly 2004).

We used *Cloudy* to predict the [O III] line emission from the outflowing gas in each of the 36 BAL components of the 30 $z < 1$ objects. Each component is characterized by a single ionization parameter and density, but is generally split into multiple bins with different column densities (Leighly et al. 2018; Choi et al. 2022). The [O III] emission was computed for each bin and then summed. The local covering fraction log$a$ for the BAL outflows was not taken into account in the computation of the [O III] flux, as it is not clear how it would manifest in the observations of line emission. The luminosity of the [O III] emission was then computed for each component assuming a global covering fraction of 10% for the line-emitting gas.

We expect the luminosity of the predicted [O III] could depend on several parameters. The [O III] flux density should be larger for higher densities. It should be larger for higher ionization parameters as a consequence of the larger column density required to include the hydrogen ionization front in FeLoBAL outflows. Both of these conditions are met in outflows closer to the central engine. However, the volume included increases as R^2 for the absorbing material for a fixed emission-line-region covering fraction. As $R^2 \propto \frac{1}{nU}$, the effects cancel out, leaving the *Cloudy* $L_{\rm [OIII]}$ uncorrelated with n, U, or R (Figure 2).

The left panel of Figure 9 shows the *Cloudy* predicted [O III] luminosity as a function of the observed [O III] luminosity. All of the predicted line emission from objects with multiple BAL outflow components are plotted with respect to the single observed [O III] luminosity. There is clearly no relationship between these two luminosities. Moreover, while both the observed and predicted [O III] luminosities each span about 1.7 dex, the ratio of the two spans almost 2.7 dex. In other words, the difference between the observed and predicted [O III] emission is not subtle.

It is possible that the observed and predicted [O III] luminosities could be reconciled if the global covering fraction of outflowing line-emitting gas were not constant for all outflows or for all emission-line regions. For example, the location of the outflow in this sample spans 3 orders of magnitude, and it is conceivable that the emission-line covering fraction is different in the vicinity of the torus ($R \sim 1$ pc) compared with on galaxy scales ($\log R \sim 3$ [pc]).

We parameterized the profound difference between the observed and predicted [O III] luminosities by defining the covering fraction correction factor. The covering fraction correction factor is the difference between the log of the *Cloudy* predicted [O III] luminosity and the log of the observed [O III] luminosity. The covering fraction correction factor measures how much larger or smaller than the assumed value of 0.1 that the covering fraction needs to be to reconcile the

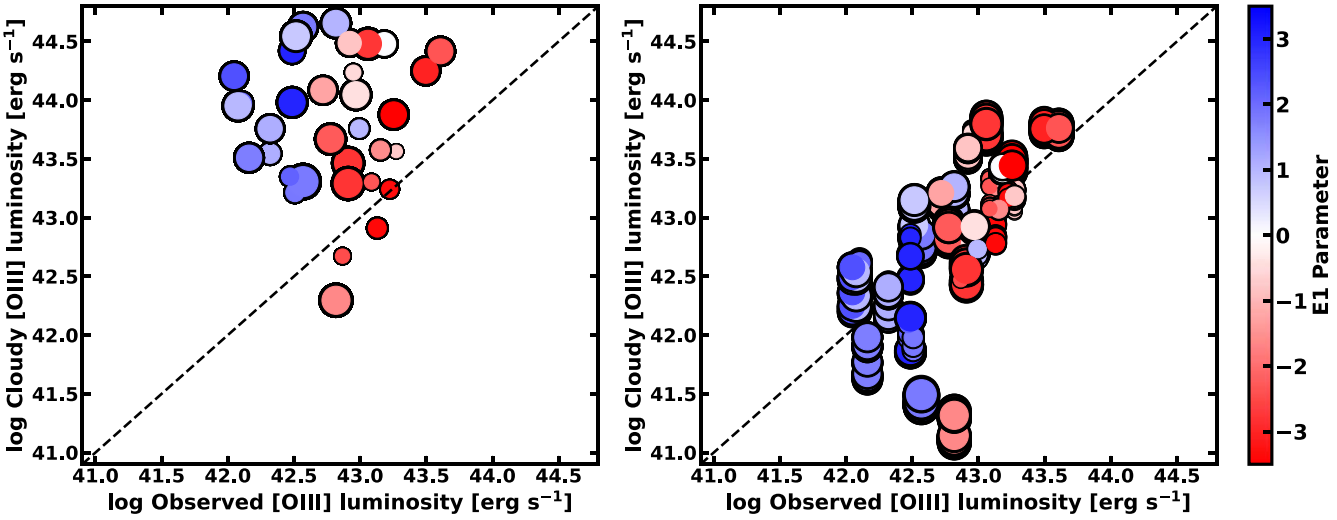

Figure 9. Inferred [O III] luminosity from the *SimBAL* models as a function of the observed [O III] luminosity. The several objects with more than one outflow component are plotted more than once. The marker color denotes the corresponding $E1$ parameter and the size of the marker corresponds to the location log$R$ parameter. *Left:* The predicted values are generally larger than the observed values, potentially implying a smaller emission-line-gas covering fraction than the assumed 10%. *Right:* The same as the left plot, with the covering fraction correction determined by the regression analysis (see text). The data were plotted using regression results for each of the 48 combinations.

observed and predicted [O III] luminosities. In Section 3.1 we showed that the covering fraction correction factor is significantly different for $E1 < 0$ versus $E1 > 0$ objects. The median values were 0.6 (1.5) for the $E1 < 0$ ($E1 > 0$) objects, respectively, implying that, on average, the emission-line region covering fraction needs to be 4 (32) times smaller than 0.1.

We explored the possibility that the covering fraction depends on other parameters using multiple regression analysis. We considered seven independent variables, and our reasons for choosing these parameters follows. We included log$R$ for the reasons outlined above. We also considered the Seyfert type using the $E1$ parameter, and the log of the estimated bolometric luminosity because there is evidence for a reduction in the [O III] emission at larger luminosities (Baskin & Laor 2005). Objects with a high Eddington ratio might produce more powerful winds and thereby evacuate a larger fraction of their reservoir of gas, so we also consider $\log L_{\rm Bol}/L_{\rm Edd}$. There is evidence that the BAL partial covering fraction log$a$ is local (Leighly et al. 2019b), but it is possible there are global trends as well. In any particular outflow component, log$a$ is a function of the velocity. For this experiment, we chose the representative log$a$ to be the one in the bin with the deepest ground-state Fe II absorption. If the velocity of the outflow is very large, then the resulting line may be very broad and blend with the continuum, so we also considered the opacity-weighted $v_{\rm off}$. Finally, the observed [O III] velocity offset might reveal a connection between the outflow and the observed emission.

The result forms a multiple regression problem with the seven independent variables listed above. As in Section 3.2, we accounted for the multiple components in five of the objects by running the regression analysis for all 48 combinations. We used `mlinmix_err` (Kelly 2007), which accounts for measurement errors in both the dependent variable (the covering fraction) and the independent variables (the design matrix) using the Pearson correlation coefficient. To determine which independent variables can best reproduce the variance in the covering fraction, the multiple regression procedure was iterated, each time removing the independent variable with the largest p value until all of the remaining variables showed a p value no larger than the cutoff, which was chosen to be 0.025.

A statistically significant correlation was found between the $E1$ parameter and the covering fraction correction factor for all 48 combinations. The next most significant parameter was log$R$ (39), followed by the velocity offset of [O III] (23). As more than half of the combinations found significant regression with the $E1$ parameter and log$R$, we proceeded to extract the regression parameters for these two parameters and all combinations.

The right panel of Figure 9 shows the results of the regression analysis between the covering fraction correction factor and the independent parameters $E1$ and log$R$. The *Cloudy* covering fraction was adjusted using the best-fitting regression parameters. Points are shown for each of the 48 combinations. The relationship between the observed and *SimBAL*-predicted [O III] emission is now linear, although considerable scatter remains.

We next examine how large the log covering fraction correction factors are and how they depend on the regression variables. The results from the regression are seen in Figure 10. The points are plotted for all 48 combinations, and the gray shaded region shows the 90% confidence regions from the `mlinmix_err` procedure. The left panel shows the results in three dimensions, while the right two panels show the two-dimensional projections for each of the regression variables. The assumed emission-line covering fraction was 0.1; so, for example, a log covering fraction correction value of 1 would imply that the covering fraction of 0.01 is needed to reconcile the observed and predicted [O III] values. Many of the $E1 > 0$ objects have large covering fraction correction factors (1.5–2), which would seem to imply that the emission-line-gas covering fraction needs to be be very small (0.001–0.003) in order to reconcile the observed and predicted [O III] emission.

In contrast, several of the loitering outflow objects ($E1 < 0$ with a low-velocity and compact outflow; Choi et al. 2022, Section 6.5, Figure 18) show very low covering fraction correction factors near zero, which means that the observed [O III] emission is consistent with being produced in the

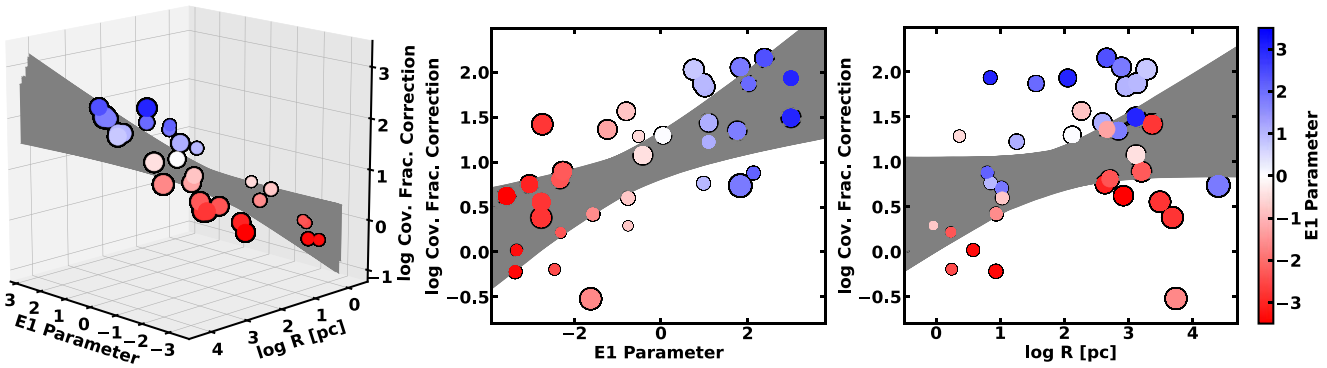

Figure 10. Covering fraction corrections inferred from the regression analysis necessary to reconcile the observed [O III] emission with that predicted to be emitted by the absorption-line gas. The assumed emission-line covering fraction was 0.1, so a log covering fraction correction value of 1 would imply that a covering fraction of 0.01 would be needed to reconcile the values. The point color represents $E1$, and the point size represents log$R$. *Left:* The multiparameter regression is a function of the $E1$ parameter and log$R$ and is therefore most accurately represented in 3D. The bow-tie surface shows the inferred errors from the `mlinmix_err` procedure; the results from all 48 combinations have been plotted. *Middle:* The results projected onto the $E1$ parameter plane. *Right:* The results projected onto the log$R$ plane.

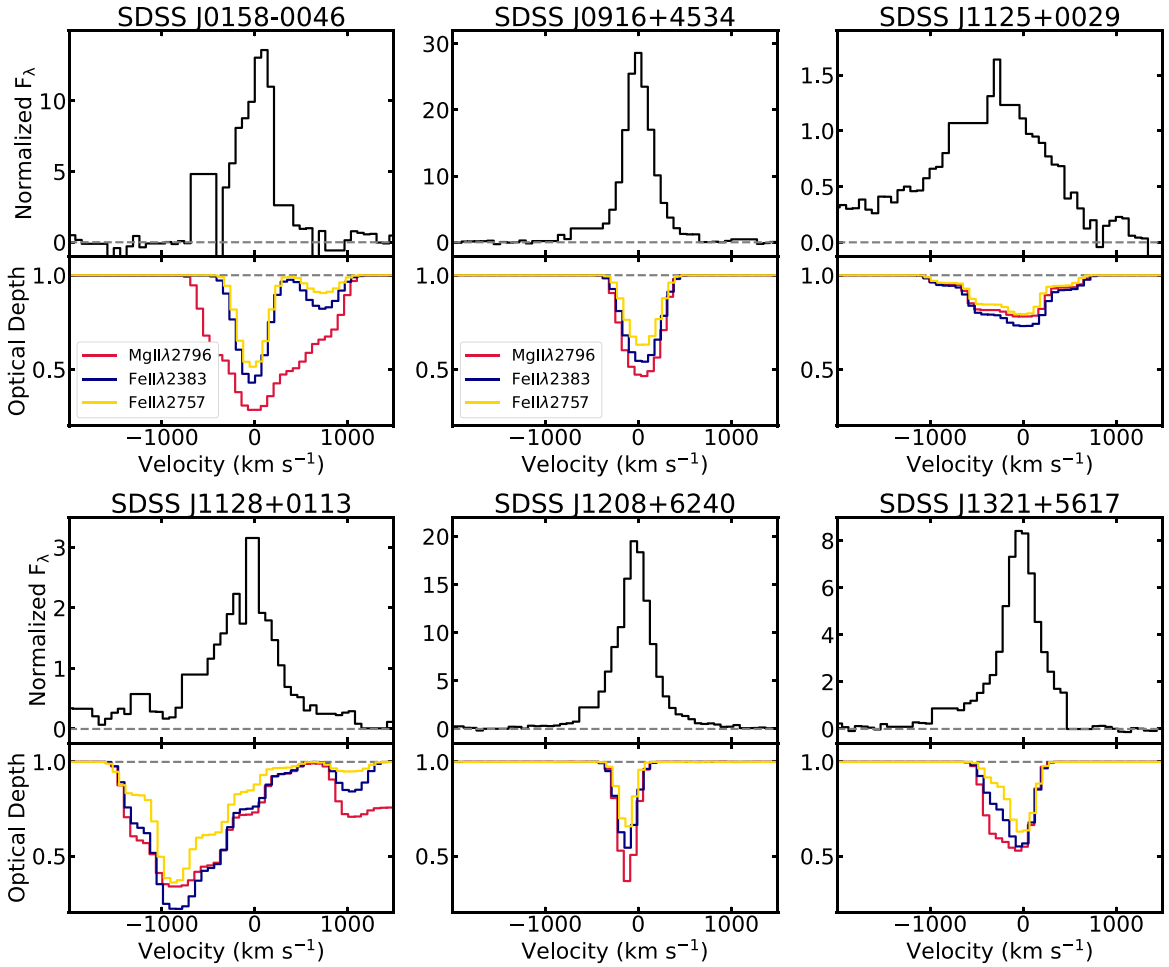

Figure 11. Comparison of the [O III]λ5008 emission profile with the absorption profile for objects with compact outflows (log$R$ < 1 [pc]) and low log covering fraction correction factors (<0.5). *Top panel in each frame:* [O III]λ5008 profile from the normalized and continuum-subtraction spectrum. *Bottom panel in each frame: SimBAL*-derived opacity profiles for ground-state Mg II, ground-state Fe II λ2883, and excited-state Fe II λ2757 taken from Figure 13 of Choi et al. 2022.

outflow. Figure 11 compares the [O III] emission profile and the absorption opacity profiles (Choi et al. 2022) for the six objects with log$R$ < 1 and log covering fraction correction less than 0.5. In these objects, the data are roughly consistent with the line emission and absorption being produced in the same gas. The profiles are not identical, but there are consistent trends: objects with broader [O III] emission lines show broader absorption profiles. For example, in SDSS J1128+0113, the [O III] line has a velocity width of $w_{80} = 830\,\mathrm{km\,s^{-1}}$ (Leighly et al. 2022), and the Mg II absorption line has a velocity width of $3000\,\mathrm{km\,s^{-1}}$ (Choi et al. 2022). In contrast, in SDSS J0916+4534, the [O III] line has a velocity width of $w_{80} = 460\,\mathrm{km\,s^{-1}}$ (Leighly et al. 2022), and the Mg II absorption line has a velocity width of $500\,\mathrm{km\,s^{-1}}$ (Choi et al. 2022).

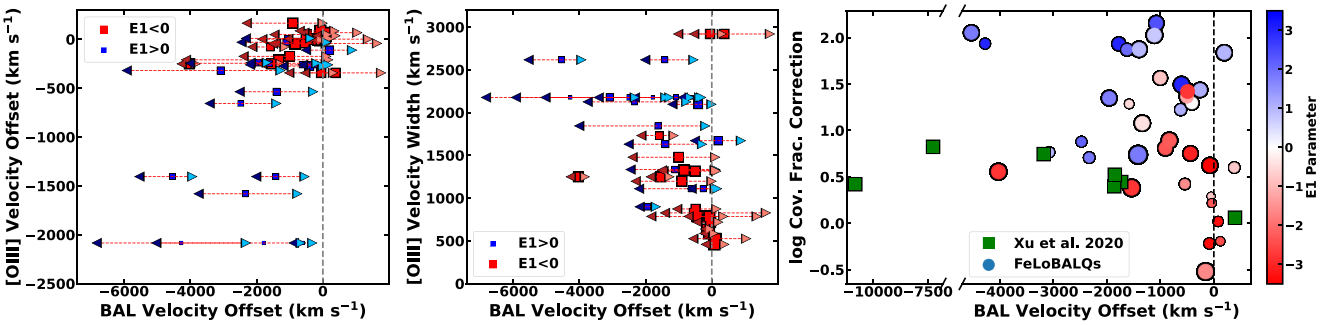

Figure 12. Comparison of the BAL velocity offset with the [O III] properties. Note that negative BAL velocities denote outflows. In the left and middle panels, the squares show the column-density weighted velocity, while the left and right triangles show the maximum and minimum speeds, respectively. The size of the square scales with the log of the [O III] equivalent width. *Left:* There is a correlation between the [O III] velocity offset and the BAL velocity offset ($p = 1.9 \times 10^{-4}$). *Middle:* There is an anticorrelation between the [O III] velocity width and the BAL velocity offset ($p = 2.7 \times 10^{-4}$). *Right:* The covering fraction correction factor is anticorrelated with the BAL velocity offset for our sample ($p = 7.8 \times 10^{-3}$) but possibly also for the Xu et al. (2020) sample. Larger velocity offsets may produce line emission that is distributed over a range of wavelengths where it may be blended with the continuum or hidden under strong Fe II emission.

SDSS J1321+5617 is particularly interesting: both the [O III] emission-line and absorption-line optical-depth profiles are narrow with a blue wing.

However, there is a flaw in this analysis. We showed in Section 4.1 that the BAL outflow velocity in some objects was much smaller than the local Keplerian velocity (Figure 5). The [O III] emission-line width in the same objects is also much less than the Keplerian velocity, by factors of 5–24. While we could explain the small outflow velocity if the orientation is directly along the line of sight, the same argument does not work for the emission lines, as they are composed of emission from all lines of sight.

The correlation analysis discussed in Section 3.2 indicates significant correlations between the BAL outflow velocity offset and the [O III] velocity offset and width (Figure 3). Figure 12 (left and middle) explores these relationships. In $E1 > 0$ objects, the [O III] emission line is sometimes very small and difficult to discern amid the sometimes strong and broad Fe II emission; therefore, points with the smallest symbols are less robustly measured. The correlation between the BAL outflow velocity and [O III] velocity offset ($p = 1.9 \times 10^{-4}$) and the anticorrelation between the BAL outflow velocity and [O III] velocity width ($p = 2.7 \times 10^{-4}$) are apparent.

Our regression analysis above explored the relationships between the observed and predicted [O III] luminosities for seven selected measurements. We also looked for relationships with other measured parameters via correlation analysis between the covering fraction correction factor and the *SimBAL* parameters (Figure 2) and the optical parameters (Figure 3). Interestingly, although the predicted [O III] emission must increase with density, we found no correlation between the covering fraction correction factor and the BAL $\log n$. This is explained by the fact that lower density BAL gas is found at larger radii, where, for a fixed global covering fraction of the line-emitting gas, the volume of the emitting gas is larger.

One correlation stands out: the outflow velocity is anticorrelated with the covering fraction correction factor. This anticorrelation is significant ($p < 0.025$) in 27 of 48 cases using Spearman's rank; it did not appear to be significant in the multiple regression analysis, as `mlinmix_err` uses Pearson's R. This dependence offers a way to reconcile the large covering-fraction correction factors required by $E1 > 0$ objects: the [O III] emitted by the BAL could be so broadened that it blends with the continuum, especially in low signal-to-noise spectra or amidst strong Fe II emission.

5. Summary and Future Work

5.1. Summary

This is the third in a sequence of four papers that discuss the properties of low-redshift FeLoBALQs. Taken together, they build a picture of the properties and physical conditions of the BAL gas and explore links between these properties to the accretion and emission-line properties of the quasars.

This paper combines *SimBAL* (Choi et al. 2022) and optical emission-line analysis (Leighly et al. 2022). The most significant result is the discovery that the $E1$ parameter division discovered by Leighly et al. (2022) carries over to the outflow properties (Section 4.1). Among the $E1 > 0$ high-accretion-rate objects, the outflow velocity *decreases* with the distance from the central engine (Figure 4). This is consistent with the expectation of radiative line driving acceleration. Among the $E1 < 0$ low-accretion-rate objects, the outflow velocity *increases* with the distance from the central engine.

We confirmed the relationship between the outflow velocity and Eddington ratio previously reported by Ganguly et al. (2007); i.e., at a particular Eddington ratio, a range of velocities are observed up to a maximum velocity, which is itself a function of the Eddington ratio (Section 4.2). Using the physical properties of the outflows obtained from the *SimBAL* analysis, we investigated whether the scatter in the velocity at a particular Eddington ratio could be a consequence of a scatter in the force multiplier or the launch radius. We found that among $E1 > 0$ objects, the scatter in the velocity could plausibly be attributed to a scatter in the launch radius, while among $E1 < 0$ objects, the scatter in the velocity could be attributed to scatter in the force multiplier.

We investigated the volume filling factor of the outflows, both for the full sample (Section 4.3.1) and for the $z < 1$ subsample (Section 4.3.2). The full sample reveals a large range of log volume filling factors, from -6 to -1. At large distances from the central engine, the log volume filling factors were less than -3, similar to those inferred in HiBALQs (e.g., Gabel et al. 2006; Hamann et al. 2011, 2013). Closer to the black hole, for $\log R \lesssim 1$, the full range of volume filling factors was found. We also found that the special BAL classes identified by Choi et al. (2022; the loitering outflows and the other overlapping trough objects) are also divided by their $E1$ parameter and, by

extension, their Eddington ratio. The loitering outflow objects have $E1 < 0$ and low Eddington ratios, while other overlapping trough objects have $E1 > 0$ and high Eddington ratios. Moreover, although both special types of FeLoBALQ outflows are compact, with typical locations of ∼10 pc from the central engine, a dramatically different number of assumed spherical clouds would be required to occult the continuum emission region (Figure 8). For the loitering outflows, a single cloud (or continuous outflow) would be sufficient. For the other overlapping trough absorbers, 100–1000 s of clouds would be required. Of course, the outflow may not have the structure of discrete spherical clouds; the point is that the differing physical conditions of these two categories of outflows tell us that the structure of the outflows is dramatically different.

We also investigated the relationship between the observed [O III] emission line and the [O III] emission predicted to be produced by the BAL outflow gas (Section 4.4). This analysis first underlines the very large range of equivalent widths observed in this sample. The observed [O III] luminosity and the estimated bolometric luminosity both span about 1.6 dex, but the ratio of the two luminosities spans 2.1 dex. We found that, in order to reconcile the observed and predicted log [O III] luminosities, the emission-line-gas global covering fraction may depend on the $E1$ parameter and the location of the outflow log$R$ (Figure 9). At the same time, the covering fraction correction factor (defined as the difference between the observed and predicted [O III] luminosity) was observed to be correlated with the outflow velocity, which may imply that the predicted strong [O III] emission in $E1 > 0$ objects is broadened and hidden under their typically strong Fe II emission (Figure 12). Most intriguing were the six $E1 < 0$ objects with the lowest covering-fraction correction factors, whose [O III] profiles resembled the BAL absorption profiles (Figure 11).

The final paper in this series of four papers (K. M. Leighly et al. in preparation) includes an analysis of the broadband optical/IR properties and discusses the potential implications for quasar evolution scenarios.

5.2. Future Work

This sample was limited to objects with redshifts less than 1.63 for the full 50 object sample from Choi et al. (2022) and less than 1.0 for the optical emission-line analysis from Leighly et al. (2022). FeLoBALQs can be observed up to $z \sim 3$ in ground-based optical-band spectra. Because the SDSS is a flux-limited survey, we generally expect higher-redshift objects to be more luminous; a sample currently being analyzed has bolometric luminosities about 1 order of magnitude larger than the $z < 1$ sample. Assuming a similar distribution of Eddington ratios, the higher-redshift objects will have larger black hole masses and therefore a softer (more UV-dominant) SED. The softer SED could influence the properties of the BAL outflows in two ways: 1) the ions present in the outflowing gas would be different, e.g., tend toward lower ionization species (e.g., Leighly et al. 2007), and 2) the velocities might be larger, as the SED will produce a relatively larger number of UV photons that can transfer momentum by resonance scattering in the outflowing gas. Preliminary analysis of a higher-redshift sample that is being observed in the near-infrared shows evidence of higher outflow velocities (Voelker et al. 2021). Another interesting feature of the high-redshift sample is that the larger redshifts provide access to the high-ionization lines (e.g., C IV, Si IV) that these objects share with the much more common HiBALQs. Preliminary analysis shows that HiBALQs seem to be very different than FeLoBALQs (Hazlett et al. 2019; Leighly et al. 2019a); in particular, the high ionization lines sometimes have complicated velocity structures and certainly extend to higher velocities. The potential link between the low-ionization line and high-ionization line properties may also prove to be very illuminating.

Our investigation of whether there could be a relationship between the ionized outflows manifest in [O III] emission and the BAL outflows showed that in most objects such a relationship would be possible only if the emission-line covering fraction is extremely low, or if the [O III] is broad and blended with the Fe II emission. An exception was several of the loitering outflow objects, where the emission-line and absorption-line profiles appeared to resemble one another. All of these objects had compact outflows, so the possibility that there is a direct relationship might be able to be tested with spatially resolved observations of the [O III] emission; unlike many quasars (e.g., Harrison et al. 2014; Bischetti et al. 2017; Vayner et al. 2021), the [O III] emission in these objects should be unresolved if it does indeed originate in the BAL outflow. Proving a relationship would be very difficult in general. However, we might be able to falsify one. At a redshift of 0.9, the angular scale is about 7.9 kpc per arcsec, so it would be possible to determine whether the [O III] emission was extended or compact on the scale of a kiloparsec. Many of the *SimBAL* solutions indicate BAL outflows with size scales much less than 1 kpc. The [O III] emission should be unresolved in such objects.

Regardless of the details, the analysis presented here has shown that again, key physical properties of the outflows differ as a function of the location in the quasar and as a function of the accretion rate as probed by the $E1$ parameter. These patterns and differences have broad potential implications. We may finally be able to understand the acceleration mechanisms that operate in quasars. In addition, we may be able to use the accretion properties measured from the emission lines to statistically infer the outflow properties in objects that do not show outflows along the line of sight. These ambitious goals will require much more work and analysis of many more objects, but at least we have identified a promising path forward.

We thank the current and past *SimBAL* group members and the anonymous referee for useful discussions and comments on the manuscript. Support for *SimBAL* development and analysis is provided by NSF Astronomy and Astrophysics grants No. 1518382, 2006771, 2007023 and. This work was performed in part at Aspen Center for Physics, which is supported by National Science Foundation grant PHY-1607611. S.C.G. thanks the Natural Science and Engineering Research Council of Canada.

Long before the University of Oklahoma was established, the land on which the University now resides was the traditional home of the “Hasinais” Caddo Nation and “Kirikiris” Wichita & Affiliated Tribes. This land was also once part of the Muscogee Creek and Seminole nations.

We acknowledge this territory once also served as a hunting ground, trade exchange point, and migration route for the Apache, Comanche, Kiowa and Osage nations. Today, 39 federally recognized Tribal nations dwell in what is now the State of Oklahoma as a result of settler colonial policies designed to assimilate Indigenous peoples.

The University of Oklahoma recognizes the historical connection our university has with its Indigenous community. We acknowledge, honor, and respect the diverse Indigenous peoples connected to this land. We fully recognize, support, and advocate for the sovereign rights of all of Oklahoma's 39 tribal nations.

This acknowledgment is aligned with our university's core value of creating a diverse and inclusive community. It is our institutional responsibility to recognize and acknowledge the people, culture and history that make up our entire OU Community.

Funding for the SDSS and SDSS-II has been provided by the Alfred P. Sloan Foundation, the Participating Institutions, the National Science Foundation, the U.S. Department of Energy, the National Aeronautics and Space Administration, the Japanese Monbukagakusho, the Max Planck Society, and the Higher Education Funding Council for England. The SDSS webite is http://www.sdss.org/.

The SDSS is managed by the Astrophysical Research Consortium for the Participating Institutions. The Participating Institutions are the American Museum of Natural History, Astrophysical Institute Potsdam, University of Basel, University of Cambridge, Case Western Reserve University, University of Chicago, Drexel University, Fermilab, the Institute for Advanced Study, the Japan Participation Group, Johns Hopkins University, the Joint Institute for Nuclear Astrophysics, the Kavli Institute for Particle Astrophysics and Cosmology, the Korean Scientist Group, the Chinese Academy of Sciences (LAMOST), Los Alamos National Laboratory, the Max-Planck-Institute for Astronomy (MPIA), the Max-Planck-Institute for Astrophysics (MPA), New Mexico State University, Ohio State University, University of Pittsburgh, University of Portsmouth, Princeton University, the United States Naval Observatory, and the University of Washington.

Funding for SDSS-III has been provided by the Alfred P. Sloan Foundation, the Participating Institutions, the National Science Foundation, and the U.S. Department of Energy Office of Science. The SDSS-III website is http://www.sdss3.org/.

SDSS-III is managed by the Astrophysical Research Consortium for the Participating Institutions of the SDSS-III Collaboration including the University of Arizona, the Brazilian Participation Group, Brookhaven National Laboratory, Carnegie Mellon University, University of Florida, the French Participation Group, the German Participation Group, Harvard University, the Instituto de Astrofisica de Canarias, the Michigan State/Notre Dame/JINA Participation Group, Johns Hopkins University, Lawrence Berkeley National Laboratory, Max Planck Institute for Astrophysics, Max Planck Institute for Extraterrestrial Physics, New Mexico State University, New York University, Ohio State University, Pennsylvania State University, University of Portsmouth, Princeton University, the Spanish Participation Group, University of Tokyo, University of Utah, Vanderbilt University, University of Virginia, University of Washington, and Yale University.

Software: Cloudy (Ferland et al. 2013), mlinmix_err (Kelly 2007), SimBAL (Leighly et al. 2018).

ORCID iDs

Hyunseop Choi (최현섭) https:/orcid.org/0000-0002-3173-1098
Karen M. Leighly https://orcid.org/0000-0002-3809-0051
Donald M. Terndrup https://orcid.org/0000-0002-0431-1645
Sarah C. Gallagher https://orcid.org/0000-0001-6217-8101
Gordon T. Richards https://orcid.org/0000-0002-1061-1804

References

Aoki, K., Oyabu, S., Dunn, J. P., et al. 2011, PASJ, 63, 457
Arav, N., Li, Z.-Y., & Begelman, M. C. 1994, ApJ, 432, 62
Arav, N., Xu, X., Miller, T., Kriss, G. A., & Plesha, R. 2020, ApJS, 247, 37
Bahk, H., Woo, J.-H., & Park, D. 2019, ApJ, 875, 50
Baskin, A., & Laor, A. 2005, MNRAS, 358, 1043
Bevington, P. R. 1969, Data Reduction and Error Analysis for the Physical Sciences (New York: McGraw-Hill)
Bischetti, M., Piconcelli, E., Vietri, G., et al. 2017, A&A, 598, A122
Boroson, T. A. 2002, ApJ, 565, 78
Boroson, T. A., & Green, R. F. 1992, ApJS, 80, 109
Brotherton, M. S., Wills, B. J., Francis, P. J., & Steidel, C. C. 1994, ApJ, 430, 495
Choi, H., Leighly, K. M., Terndrup, D. M., et al. 2022, arXiv:2203.11964
Choi, H., Leighly, K. M., Terndrup, D. M., Gallagher, S. C., & Richards, G. T. 2020, ApJ, 891, 53
Coatman, L., Hewett, P. C., Banerji, M., et al. 2017, MNRAS, 465, 2120
Corbin, M. R., & Boroson, T. A. 1996, ApJS, 107, 69
de Kool, M., Arav, N., Becker, R. H., et al. 2001, ApJ, 548, 609
de Kool, M., Becker, R. H., Arav, N., Gregg, M. D., & White, R. L. 2002a, ApJ, 570, 514
de Kool, M., Becker, R. H., Gregg, M. D., White, R. L., & Arav, N. 2002b, ApJ, 567, 58
de Kool, M., & Begelman, M. C. 1995, ApJ, 455, 448
Di Matteo, T., Springel, V., & Hernquist, L. 2005, Natur, 433, 604
Dunn, J. P., Bautista, M., Arav, N., et al. 2010, ApJ, 709, 611
Elitzur, M., & Netzer, H. 2016, MNRAS, 459, 585
Faucher-Giguère, C.-A., Quataert, E., & Murray, N. 2012, MNRAS, 420, 1347
Ferland, G. J., Porter, R. L., van Hoof, P. A. M., et al. 2013, RMxAA, 49, 137
Fiore, F., Feruglio, C., Shankar, F., et al. 2017, A&A, 601, A143
Foreman-Mackey, D., Hogg, D. W., Lang, D., & Goodman, J. 2013, PASP, 125, 306
Francis, P. J., Hewett, P. C., Foltz, C. B., & Chaffee, F. H. 1992, ApJ, 398, 476
Frank, J., King, A., & Raine, D. J. 2002, Accretion Power in Astrophysics: Third Edition (Cambridge: Cambridge Univ. Press)
Gabel, J. R., Arav, N., & Kim, T.-S. 2006, ApJ, 646, 742
Gallagher, S. C., Richards, G. T., Lacy, M., et al. 2007, ApJ, 661, 30
Ganguly, R., Brotherton, M. S., Cales, S., et al. 2007, ApJ, 665, 990
Gibson, R. R., Jiang, L., Brandt, W. N., et al. 2009, ApJ, 692, 758
Giustini, M., & Proga, D. 2019, A&A, 630, A94
Glikman, E. 2017, RNAAS, 1, 48
Glikman, E., Lacy, M., LaMassa, S., et al. 2018, ApJ, 861, 37
Grupe, D. 2004, AJ, 127, 1799
Hall, P. B., Anderson, S. F., Strauss, M. A., et al. 2002, ApJS, 141, 267
Hamann, F. 1998, ApJ, 500, 798
Hamann, F., Chartas, G., McGraw, S., et al. 2013, MNRAS, 435, 133
Hamann, F., Kanekar, N., Prochaska, J. X., et al. 2011, MNRAS, 410, 1957
Hamann, F., Tripp, T. M., Rupke, D., & Veilleux, S. 2019, MNRAS, 487, 5041
Harrison, C. M., Alexander, D. M., Mullaney, J. R., & Swinbank, A. M. 2014, MNRAS, 441, 3306
Hazlett, R., Leighly, K., Dabbieri, C., et al. 2019, AAS Meeting, 233, 242.41
Hewett, P. C., & Foltz, C. B. 2003, AJ, 125, 1784
Hopkins, P. F., & Elvis, M. 2010, MNRAS, 401, 7
Ishibashi, W., Banerji, M., & Fabian, A. C. 2017, MNRAS, 469, 1496
Kelly, B. C. 2007, ApJ, 665, 1489
Knigge, C., Scaringi, S., Goad, M. R., & Cottis, C. E. 2008, MNRAS, 386, 1426
Korista, K. T., Bautista, M. A., Arav, N., et al. 2008, ApJ, 688, 108
Krawczyk, C. M., Richards, G. T., Gallagher, S. C., et al. 2015, AJ, 149, 203
Laor, A., & Brandt, W. N. 2002, ApJ, 569, 641
Leighly, K., Terndrup, D., Gallagher, S. C., & Richards, G. 2019a, AAS Meeting, 233, 242.39
Leighly, K. M., Terndrup, D. M., Lucy, A. B., et al. 2019b, ApJ, 879, 27
Leighly, K. M. 2004, ApJ, 611, 125
Leighly, K. M., Choi, H., DeFrancesco, C., et al. 2022, ApJ, 935, 92
Leighly, K. M., Halpern, J. P., Jenkins, E. B., & Casebeer, D. 2007, ApJS, 173, 1

Leighly, K. M., Hamann, F., Casebeer, D. A., & Grupe, D. 2009, ApJ, 701, 176
Leighly, K. M., Terndrup, D. M., Gallagher, S. C., Richards, G. T., & Dietrich, M. 2018, ApJ, 866, 7
Lucy, A. B., Leighly, K. M., Terndrup, D. M., Dietrich, M., & Gallagher, S. C. 2014, ApJ, 783, 58
Ludwig, R. R., Wills, B., Greene, J. E., & Robinson, E. L. 2009, ApJ, 706, 995
Miller, T. R., Arav, N., Xu, X., & Kriss, G. A. 2020, MNRAS, 499, 1522
Misawa, T., Charlton, J. C., Eracleous, M., et al. 2007, ApJS, 171, 1
Moe, M., Arav, N., Bautista, M. A., & Korista, K. T. 2009, ApJ, 706, 525
Murray, N., & Chiang, J. 1997, ApJ, 474, 91
Osterbrock, D. E., & Ferland, G. J. 2006, Astrophysics of Gaseous Nebulae and Active Galactic Nuclei (Mill Valley, CA: Univ. Science Books)
Pâris, I., Petitjean, P., Aubourg, É., et al. 2018, A&A, 613, A51
Proga, D., & Waters, T. 2015, ApJ, 804, 137
Rankine, A. L., Hewett, P. C., Banerji, M., & Richards, G. T. 2020, MNRAS, 492, 4553
Reichard, T. A., Richards, G. T., Hall, P. B., et al. 2003, AJ, 126, 2594
Revalski, M., Meena, B., Martinez, F., et al. 2021, ApJ, 910, 139
Runnoe, J. C., Ganguly, R., Brotherton, M. S., & DiPompeo, M. A. 2013, MNRAS, 433, 1778
Schulze, A., Misawa, T., Zuo, W., et al. 2018, ApJ, 853, 167
Shen, Y. 2016, ApJ, 817, 55
Shen, Y., & Ho, L. C. 2014, Natur, 513, 210
Shen, Y., Richards, G. T., Strauss, M. A., et al. 2011, ApJS, 194, 45
Shi, X.-H., Jiang, P., Wang, H.-Y., et al. 2016, ApJ, 829, 96
Stern, J., & Laor, A. 2012, MNRAS, 426, 2703
Sulentic, J. W., Marziani, P., & Dultzin-Hacyan, D. 2000, ARA&A, 38, 521
Thompson, T. A., Fabian, A. C., Quataert, E., & Murray, N. 2015, MNRAS, 449, 147
Tolea, A., Krolik, J. H., & Tsvetanov, Z. 2002, ApJL, 578, L31
Trump, J. R., Hall, P. B., Reichard, T. A., et al. 2006, ApJS, 165, 1
Urrutia, T., Becker, R. H., White, R. L., et al. 2009, ApJ, 698, 1095
Vayner, A., Wright, S. A., Murray, N., et al. 2021, ApJ, 919, 122
Voelker, J., Choi, H., Leighly, K., DeFrancesco, C., & Dabbieri, C. 2021, AAS Meeting, 237, 337.10
Wang, J., Wei, J. Y., & He, X. T. 2006, ApJ, 638, 106
Waters, T., & Proga, D. 2019, ApJ, 875, 158
Wills, B. J., Laor, A., Brotherton, M. S., et al. 1999, ApJL, 515, L53
Wolf, J., Salvato, M., Coffey, D., et al. 2020, MNRAS, 492, 3580
Xu, X., Zakamska, N. L., Arav, N., Miller, T., & Benn, C. 2020, MNRAS, 495, 305
Yip, C. W., Connolly, A. J., Vanden Berk, D. E., et al. 2004, AJ, 128, 2603
Yuan, M. J., & Wills, B. J. 2003, ApJL, 593, L11
Zakamska, N. L., & Greene, J. E. 2014, MNRAS, 442, 784